

AD-A126 116

THEORY OF CUSPTRON MICROWAVE TUBES(U) NAVAL SURFACE
WEAPONS CENTER SILVER SPRING MD H S UHM ET AL. OCT 82
NSWC/TR-82-530 SBI-AD-F580 147

1/1

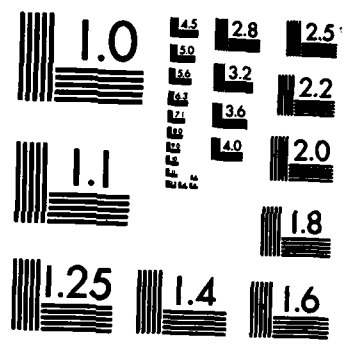
UNCLASSIFIED

F/G 9/1

NL

END

FILED
21
afc



MICROCOPY RESOLUTION TEST CHART
NATIONAL BUREAU OF STANDARDS-1963-A

ADA 126116

NSWC TR 82-538
PLASMA PHYSICS PUBLICATION NO. 25-23

THEORY OF CUSPTRON MICROWAVE TUBES

BY HAN S. UHM,
CHUNG M. KIM

RESEARCH AND TECHNOLOGY DEPARTMENT

OCTOBER 1982

Approved for public release, distribution unlimited.

DTIC
MAR 17 1983
H

DTIC FILE COPY



NAVAL SURFACE WEAPONS CENTER

Dahlgren, Virginia 22448 • Silver Spring, Maryland 20910

83 03 18 024

UNCLASSIFIED

SECURITY CLASSIFICATION OF THIS PAGE (When Data Entered)

REPORT DOCUMENTATION PAGE		READ INSTRUCTIONS BEFORE COMPLETING FORM
1. REPORT NUMBER NSWC TR 82-530	2. GOVT ACCESSION NO. ADA126 116	3. RECIPIENT'S CATALOG NUMBER
4. TITLE (and Subtitle) THEORY OF CUSPTRON MICROWAVE TUBES		5. TYPE OF REPORT & PERIOD COVERED
		6. PERFORMING ORG. REPORT NUMBER
7. AUTHOR(s) Han S. Uhm and Chung M. Kim		8. CONTRACT OR GRANT NUMBER(s)
9. PERFORMING ORGANIZATION NAME AND ADDRESS Naval Surface Weapons Center (Code R41) White Oak Silver Spring, MD 20910		10. PROGRAM ELEMENT, PROJECT, TASK AREA & WORK UNIT NUMBERS 61152N; ZR00001; ZR01109; R01AA400
11. CONTROLLING OFFICE NAME AND ADDRESS		12. REPORT DATE October 1982
		13. NUMBER OF PAGES 70
14. MONITORING AGENCY NAME & ADDRESS (if different from Controlling Office)		15. SECURITY CLASS. (of this report) UNCLASSIFIED
		15a. DECLASSIFICATION/DOWNGRADING SCHEDULE
16. DISTRIBUTION STATEMENT (of this Report) Approved for public release; distribution unlimited.		
17. DISTRIBUTION STATEMENT (of the abstract entered in Block 20, if different from Report)		
18. SUPPLEMENTARY NOTES		
19. KEY WORDS (Continue on reverse side if necessary and identify by block number) Cusptron Microwave Tubes		
20. ABSTRACT (Continue on reverse side if necessary and identify by block number) Stability properties of the negative-mass instability in a rotating annular electron beam (E-layer) is investigated, in connection with applications on the cusptron microwave tubes. Analysis is carried out for an infinitely long E-layer propagating through a magnetron-type conducting wall and propagating parallel to an applied axial magnetic field. We assume that the E-layer is thin and very tenuous. A closed algebraic dispersion relation of the negative-mass instability is obtained, including the important influence of		

DD FORM 1473
1 JAN 73EDITION OF 1 NOV 65 IS OBSOLETE
S/N 0102-LF-014-6401

UNCLASSIFIED

SECURITY CLASSIFICATION OF THIS PAGE (When Data Entered)

UNCLASSIFIED

SECURITY CLASSIFICATION OF THIS PAGE (When Data Entered)

conducting boundaries on the mode control in microwave generation and amplification. It is shown that for typical present experimental beam parameters, gain and efficiency of the cusptron can be more than five times those of the gyrotron. Moreover, with an appropriate geometric configuration, perturbations with azimuthal mode number N can be dominantly unstable, thereby optimizing the microwave power output for radiation with high frequency $\omega \approx N\omega_c$, where ω_c is the electron cyclotron frequency and N is the resonator number in the conducting wall.



Accession For	
NTIS GRA&I	<input checked="" type="checkbox"/>
DTIC TAB	<input type="checkbox"/>
Unannounced	<input type="checkbox"/>
Justification	
By _____	
Distribution/	
Availability Codes	
Dist	Avail and/or
A	Special

UNCLASSIFIED

SECURITY CLASSIFICATION OF THIS PAGE (When Data Entered)

FOREWORD

Stability properties of the negative-mass instability in a rotating annular electron beam (E-layer) is investigated, in connection with applications on the cusptron microwave tubes. Analysis is carried out for an infinitely long E-layer propagating through a magnetron-type conducting wall and propagating parallel to an applied axial magnetic field. We assume that the E-layer is thin and very tenuous. A closed algebraic dispersion relation of the negative-mass instability is obtained, including the important influence of conducting boundaries on the mode control in microwave generation and amplification. It is shown that for typical present experimental beam parameters, gain and efficiency of the cusptron can be more than five times those of the gyrotron. Moreover, with an appropriate geometric configuration, perturbations with azimuthal mode number N can be dominantly unstable, thereby optimizing the microwave power output for radiation with high frequency $\omega \approx N\omega_c$, where ω_c is the electron cyclotron frequency and N is the resonator number in the conducting wall.

Approved by:



IRA M. BLATSTEIN, Head
Radiation Division

CONTENTS

<u>Section</u>		<u>Page</u>
I	INTRODUCTION	1
II	VLASOV-MAXWELL THEORY	4
III	VACUUM DISPERSION RELATION	15
IV	NEGATIVE-MASS INSTABILITY IN MAGNETRON-TYPE CONDUCTOR	18
V	CONCLUSIONS	27
VI	ACKNOWLEDGEMENTS	29
	APPENDIX A--MAGNETIC WAVE ADMITTANCES	A-1

ILLUSTRATIONS

<u>Figure</u>		<u>Page</u>
1	CROSS SECTIONAL VIEW OF CUSPTRON	30
2	PLOTS OF THE PARAMETERS η (SOLID CURVES) and ζ (DASHED CURVES) VERSUS RATIO R_c/R_a [OBTAINED FROM EQ. (45)] FOR $N = 6$, $s = 0$, $\alpha = \pi/12$ AND THREE LOWEST RADIAL MODES	31
3	PLOTS OF PARAMETER η VERSUS RATIO R_c/R_a OBTAINED FROM EQ. (45) FOR $s = 0$, $\alpha = \pi/2N$, LOWEST RADIAL MODE NUMBER, AND SEVERAL VALUES OF N	32
4	PLOTS OF PARAMETER η VERSUS RATIO R_c/R_a OBTAINED FROM EQ. (45) FOR $N = 6$, $\alpha = \pi/12$, LOWEST RADIAL MODE NUMBER AND DIFFERENT VALUES OF s	33
5	PLOTS OF PARAMETER η VERSUS RATIO R_c/R_a OBTAINED FROM EQ. (45) FOR $N = 8$, $s = 0$, LOWEST RADIAL MODE NUMBER AND SEVERAL VALUES OF α	34
6	THE STRAIGHT LINES $\omega = k\beta_z c + \ell\omega_c$ AND $\omega = kc/\beta_z$ INTERSECT AT $(\omega_0, k_0) = (\ell\omega_c \gamma_z^2, \ell\omega_c \beta_z \gamma_z^2/c)$. THE VACUUM WAVEGUIDE MODE $\omega = (k^2 c^2 + \eta^2 c^2/R_a^2)^{1/2}$ PASSES THROUGH (ω_0, k_0) PROVIDED $R_a \omega_c/c = \eta/\ell\gamma_z$	35
7	PLOT OF THE GEOMETRIC FACTOR $\Gamma(\omega, k_b)$ VERSUS NORMALIZED FREQUENCY ω/ω_c IN EQ. (28) FOR $N = 6$, $\ell = 6$, $s = 0$, $\alpha = \pi/12$, $R_c/R_a = 1.4$ AND $R_a \omega_c/c = 0.4433$ CORRESPONDING TO THE GRAZING CONDITION FOR $\beta_z = 0.2$	36
8	PLOTS OF (a) NORMALIZED GROWTH RATE Ω_1/ω_c AND DOPPLER-SHIFTED REAL OSCILLATION FREQUENCY Ω_r/ω_c VERSUS ω/ω_c OBTAINED FROM EQ. (47) FOR ELECTRON BEAM PARAMETERS $v = 0.002$, $\Delta = 0.04$, $\beta_\theta = 0.4$, $\beta_z = 0.2$, FIELD INDEX $n = 0$ AND THE GRAZING CONDITIONS CORRESPONDING TO EQ. (53), AND PARAMETERS OTHERWISE IDENTICAL TO FIG. 7	37

ILLUSTRATIONS (Cont.)

<u>Figure</u>		<u>Page</u>
9	PLOTS OF (a) NORMALIZED GROWTH RATE Ω_1/ω_c AND (b) DOPPLER-SHIFTED REAL OSCILLATION FREQUENCY Ω_r/ω_c VERSUS ω/ω_c OBTAINED FROM EQ. (47) FOR $R_c/R_a = 1.4$, $R_a\omega_c/c = 0.4433$, SEVERAL DIFFERENT VALUES OF THE FIELD INDEX n , AND PARAMETERS OTHERWISE IDENTICAL TO FIG. 8	39
10	PLOTS OF (a) NORMALIZED GROWTH RATE Ω_1/ω_c AND (b) DOPPLER-SHIFTED REAL FREQUENCY Ω_r/ω_c VERSUS NORMALIZED AXIAL WAVE NUMBER kc/ω_c OBTAINED FROM EQ. (48) FOR THE PARAMETERS IDENTICAL TO FIG. 8	41
11	PLOTS OF (a) NORMALIZED GROWTH RATE Ω_1/ω_c AND (b) DOPPLER-SHIFTED REAL FREQUENCY Ω_r/ω_c VERSUS ω/ω_c FOR $\beta_\theta = 0.96$, THE GRAZING CONDITIONS CORRESPONDING TO EQ. (53), AND PARAMETERS OTHERWISE IDENTICAL TO FIG. 8	43
12	PLOT OF THE NORMALIZED GROWTH RATE Ω_1/ω_c VERSUS ω/ω_c OBTAINED FROM EQS. (47) AND (58) FOR $\beta_\theta = 0.96$, $N = 24$, $l = 25$, $R_c/R_a = 1.1$, $R_a\omega_c/c = 1.069$, $\alpha = \pi/2N$, AND PARAMETERS OTHERWISE IDENTICAL TO FIG. 8	45
A-1	CONFIGURATION OF A RESONATOR	A-6

I. INTRODUCTION

In recent years, there have been numerous experimental and theoretical investigations on high power and high frequency microwave devices such as gyrotrons,¹⁻³ relativistic magnetrons⁴ and free electron lasers.^{5,6} High power microwaves have been also produced by the negative-mass instability⁷⁻⁹ of a relativistic rotating electron layer (E-layer) in a conducting waveguide. This relatively new scheme of microwave generation by a rotating E-layer has many attractive features in practical application. Using the mode control scheme currently under investigation,¹⁰ for example, this device could be a tunable, high-frequency microwave tube with low magnetic fields. One of the simple ways to produce a rotating E-layer is use of a magnetic cusp field through which an annular electron beam becomes the same radius rotating beam.¹¹ After passing through a cusped magnetic field, a nonrelativistic E-layer is propagating through a conventional magnetron-type conducting wall called the cusptron. The name "cusptron" is originated from the cusp and the magnetron. In this paper, we investigate the negative-mass stability properties of the E-layer in a magnetron-type conductor, in connection with the application on the cusptron microwave tube.

The stability analysis of the negative-mass instability is carried out for an E-layer with radius R_0 propagating through a magnetron-type conductor with its inner-and outer-most radii R_a and R_c , respectively. Equilibrium and stability properties are calculated for the electron distribution function [Eq. (1)] in which all electrons have the same energy and the same canonical angular momentum but a Lorentzian

distribution in the axial canonical momentum. The stability analysis is calculated within the framework of the linearized Vlasov-Maxwell equations for an infinitely long E-layer propagating parallel to an applied magnetic field $B_0 \hat{e}_z$ with an axial velocity $\beta_z c \hat{e}_z$. We assume that the E-layer is thin and very tenuous. The formal dispersion relation [Eq. (29)] of the negative-mass instability is obtained in Section II, including the important influence of conducting boundaries on the mode control in microwave amplification and generation.

In Section III, properties of the vacuum dispersion relation in a magnetron-type conductor are investigated without including the influence of beam electrons. It is shown that the vacuum dispersion relation reduces to three destructive modes; the transverse electric (TE), the transverse magnetic (TM), and the magnetron TE modes. From numerical calculation, the cut-off frequency $\omega_{ct} = \eta c/R_a$ is obtained in terms of the ratio R_c/R_a . In Section IV, the negative-mass stability properties of an E-layer is numerically investigated. Several points are noteworthy from the numerical calculation for a nonrelativistic cusptron. First, optimum coupling occurs between the beam and the fundamental 2π modes. It is shown for the fundamental 2π mode that for typical present experimental beam parameters, gain and efficiency of the cusptron can be more than five times those of the gyrotron. Second, for the applied magnetic field satisfying the grazing condition of the $l = N$ perturbations, other azimuthal perturbations with $l \neq N$ are suppressed. Here l is the azimuthal harmonic number of perturbations and N is the number of resonator in the magnetron-type conductor. Under this grazing condition, the $l = N$ mode perturbation is the dominant unstable mode, optimizing the microwave power output for radiation with frequency $\omega \approx l\omega_c$. Therefore, even for relatively low magnetic field, high frequency

microwave can be amplified by making use of the cusptron with $N \geq 2$. Finally, the growth rate and Doppler-shifted real oscillation frequency are substantially increased by changing the applied field index from zero to a small positive value. Preliminary investigation of a relativistic cusptron amplifier is also carried out in Section IV.

II. VLASOV-MAXWELL THEORY

As illustrated in Fig. 1, the equilibrium configuration consists of a nonneutral electron layer (E-layer) that is infinite in axial extent and aligned parallel to an applied magnetic field $B_0(r)\hat{e}_z$. The electron layer is accomplished by passing of a hollow electron beam through an ideal cusp magnetic field.¹¹ Therefore, the electron layer is in a fast rotational equilibrium, where all electrons have positive canonical angular momentum. The mean radius of the E-layer is denoted by R_0 . We also assume that the radial thickness of the E-layer is $2a$ which is much less than the equilibrium radius R_0 , i.e., $a \ll R_0$. The mean motion of the E-layer is in the azimuthal direction, and the applied magnetic field provides radial confinement of the electrons. As shown in Fig. 1, the outer conductor is a magnetron-type configuration with its inner- and outer-most radii R_a and R_c , respectively. The angle of the open spaces in the magnetron-type conductor is denoted by 2α . In the theoretical analysis, cylindrical polar coordinates (r, θ, z) are employed. In the present analysis, we assume that $v/\hat{\gamma} \ll 1$, where $v = N_b e^2 / mc^2$ is Budker's parameter and $\hat{\gamma} mc^2$ is the electron energy. Here N_b is the total number of electrons per unit axial length, $-e$ and m are the charge and rest mass of electrons, respectively. Consistent with the low-density assumption, we neglect the influence of equilibrium self-fields.

In the present analysis, we investigate the equilibrium and stability properties for the choice of equilibrium distribution function

$$f_b^0(H, P_\theta, P_z) = \frac{\omega_c N_b \hat{\gamma} \Delta}{4\pi^3 mc^2} \frac{\delta(\gamma - \hat{\gamma}) \delta(P_\theta - P_0)}{(P_z - \hat{p}_z)^2 + \hat{p}_z^2 \Delta^2} \quad (1)$$

where $H = \gamma mc^2 = (m^2 c^4 + c^2 p^2)^{1/2}$ is the total energy, P_z is the axial canonical momentum, $P_\theta = r[p_\theta - (e/c)A_0(r)]$ is the canonical angular momentum, $\omega_c = eB_0(R_0)/\gamma mc$ is the electron cyclotron frequency, $A_0(r)$ is the axial component of the equilibrium vector potential, $P_0 = (e/c)R_0 A_0(R_0) = (e/2c)R_0^2 B_0(R_0)$ and $\hat{\gamma}$, \hat{p}_z and Δ constants.

In the subsequent stability analysis, we examine the linearized Vlasov-Maxwell equations for perturbations about a thin E-layer equilibrium described by Eq. (1). To calculate stability quantities of the E-layer, we adopt a normal-mode approach in which all E-layer perturbations are assumed to vary with time and space according to

$$\delta\psi(\underline{x}, t) = \psi_\ell(r) \exp \{i(\ell\theta + kz - \omega t)\},$$

where $\text{Im}\omega > 0$. Here, ω is the complex eigenfrequency, k is the axial wavenumber, and ℓ is the azimuthal harmonic number. The Maxwell equations for the perturbed electric and magnetic field amplitudes can be expressed as

$$\begin{aligned} \underline{\nabla} \times \underline{\hat{E}}(\underline{x}) &= i(\omega/c)\underline{\hat{B}}(\underline{x}), \\ \underline{\nabla} \times \underline{\hat{B}}(\underline{x}) &= (4\pi/c)\underline{\hat{J}}(\underline{x}) - i(\omega/c)\underline{\hat{E}}(\underline{x}), \end{aligned} \quad (2)$$

where $\underline{\hat{E}}(\underline{x})$ and $\underline{\hat{B}}(\underline{x})$ are the perturbed electric and magnetic fields,

$$\underline{\hat{J}}(\underline{x}) = -e \int d^3p \underline{v} \hat{f}_b(\underline{x}, p) \quad (3)$$

is the perturbed current density.

$$\hat{f}_b(\underline{x}, p) = e \int_{-\infty}^0 dt \exp(-i\omega t) \left[\underline{\hat{E}}(\underline{x}') + \frac{\underline{v}' \times \underline{\hat{B}}(\underline{x}')}{c} \right] \frac{\partial}{\partial p'} f_b^0 \quad (4)$$

is the perturbed distribution function, and $\tau = t' - t$.

From Eq. (2), it is straightforward to show that

$$\frac{\partial}{\partial r} \hat{B}_{\ell z}(r) - i \frac{c}{\omega} \left[p^2 \hat{E}_{\ell \theta}(r) + \frac{\ell k}{r} \hat{E}_{\ell z}(r) \right] = -\frac{4\pi}{c} \hat{J}_{\ell \theta}(r) \quad (5)$$

where

$$p^2 = \omega^2/c^2 - k^2. \quad (6)$$

For present purpose, we assume that

$$|\Omega| = |\omega - \ell\omega_c - k\beta_z c| \ll \omega_c,$$

$$\ell a \ll R_0 \quad (7)$$

where $\beta_z = \hat{p}_z/\hat{\gamma}mc$ and c is the speed of light in vacuo. The perturbed axial and azimuthal electric fields [$\hat{E}_{\ell \theta}(r)$ and $\hat{E}_{\ell z}(r)$] are continuous across the beam boundaries ($r = R_1$ and $r = R_2$). Here $R_1 = R_0 - a$ and $R_2 = R_0 + a$ are the inner and outer boundaries of the E-layer, respectively. Moreover, within the context of Eq. (7), it is valid to approximate

$$\hat{E}_{\ell \theta}(R_1) \approx \hat{E}_{\ell \theta}(R_0) \approx \hat{E}_{\ell \theta}(R_2), \quad (8)$$

$$\hat{E}_{\ell z}(R_1) \approx \hat{E}_{\ell z}(R_0) \approx \hat{E}_{\ell z}(R_2).$$

Integrating Eq. (5) from $r = R_1 - \delta$ to $r = R_2 + \delta$ and taking the limit $\delta \rightarrow 0_+$, we obtain

$$\hat{B}_{\ell z}(R_2^+) - \hat{B}_{\ell z}(R_1^-) = -\frac{4\pi}{c} \int_{R_1}^{R_2} dr \hat{J}_{\ell \theta}(r), \quad (9)$$

where $\psi(R_j^\pm)$ denotes $\lim_{\delta \rightarrow 0_+} \psi(R_j \pm \delta)$. Similarly, the discontinuity of the azimuthal component of the perturbed magnetic field is given by

$$\hat{B}_{\ell\theta}(R_2^+) - \hat{B}_{\ell\theta}(R_1^-) = \frac{4\pi}{c} \int_{R_1}^{R_2} dr \hat{J}_{\ell z}(r), \quad (10)$$

For convenience in the subsequent analysis, we introduce the normalized electric and magnetic wave admittances,¹² d_{\pm} and b_{\pm} , defined at the inner and outer surfaces of the E-layer by

$$d_+ = - \left[r(\partial/\partial r) \hat{E}_{\ell z}(r) \right]_{R_2^+} / \ell \hat{E}_{\ell z}(R_2), \quad (11)$$

$$d_- = \left[r(\partial/\partial r) \hat{E}_{\ell z}(r) \right]_{R_1^-} / \ell \hat{E}_{\ell z}(R_1),$$

and

$$b_+ = - \ell \hat{B}_{\ell z}(R_2^+) / \left[r(\partial/\partial r) \hat{B}_{\ell z}(r) \right]_{R_2}, \quad (12)$$

$$b_- = \ell \hat{B}_{\ell z}(R_1^-) / \left[r(\partial/\partial r) \hat{B}_{\ell z}(r) \right]_{R_1}.$$

From Eq. (2), it is straightforward to show that

$$\frac{\partial}{\partial r} \hat{B}_{\ell z}(r) = i \frac{c}{\omega} \left[p^2 \hat{E}_{\ell\theta}(r) + \frac{\ell k}{r} \hat{E}_{\ell z}(r) \right],$$

$$\hat{B}_{\ell\theta}(r) = - \frac{k \ell}{p^2 r} \hat{B}_{\ell z}(r) + \frac{i \omega}{c p^2} \frac{\partial}{\partial r} \hat{E}_{\ell z}(r), \quad (13)$$

outside the E-layer and the radial coordinate r satisfying $r \ll R_a$.

Substituting Eq. (13) into Eqs. (9) and (10) and making use of Eqs. (11)

and (12) we obtain

$$(b_- + b_+) \left[v^2 R_0 \hat{E}_{\ell\theta}(R_0) + k\ell \hat{E}_{\ell z}(R_0) \right] = -1 \frac{4\pi\omega\ell}{c^2} \int_{R_1}^{R_2} dr \hat{J}_{\ell\theta}(r), \quad (14)$$

$$(d_- + d_+) \hat{E}_{\ell z}(R_0) = -1 \frac{4\pi k}{\omega} \int_{R_1}^{R_2} dr \hat{J}_{\ell\theta}(r) + 1 \frac{4\pi p^2 R_0}{\omega\ell} \int_{R_1}^{R_2} dr \hat{J}_{\ell z}(r),$$

where use has been made of Eq. (8). Evidently, an evaluation of the azimuthal and axial components of the perturbed current density ($\hat{J}_{\ell\theta}$ and $\hat{J}_{\ell z}$) is required for a detailed stability analysis.

A. Perturbed Current Density

In this section, we evaluate the perturbed distribution function and subsequently the perturbed current density. As indicated in Eq. (4), the particle trajectories, $r'(\tau)$, $\theta'(\tau)$ and $z'(\tau)$, in the equilibrium fields are required in order to evaluate the perturbed distribution function. The applied axial magnetic field $B_0(r)\hat{e}_z$ is approximated by

$$B_0(r) = B_0(R_0) \left(1 - n\rho/R_0 \right) \quad (15)$$

where $\rho = r - R_0$ and

$$n = - \frac{R_0}{B_0(R_0)} \left[\frac{\partial}{\partial r} B_0(r) \right]_{R_0} \quad (16)$$

is the magnetic field index. Therefore, the azimuthal component of the vector potential is expressed as

$$rA_\theta(r) = R_0 A_\theta(R_0) + B_0(R_0) \int_{R_0}^r dr r \left(1 - \frac{n\rho}{R_0} \right). \quad (17)$$

Making use of the Hamiltonian $H = \gamma m c^2 = (m^2 c^4 + c^2 p^2)^{1/2}$, the canonical angular momentum $P_\theta = r \left[p_\theta - (e/c)A_0(r) \right]$ and Eq. (17), we obtain the electron trajectories¹³

$$\begin{aligned} \rho' &= r' - R_0 = \omega_c \delta P_\theta / \hat{\gamma} m \omega_r^2 R_0 + A_r \sin(\omega_r \tau + \phi) , \\ z' &= z + p_z \tau / \hat{\gamma} m , \\ \theta' &= \omega_c - \mu \frac{\delta P_\theta}{\hat{\gamma} m R_0^2} + \frac{\omega_c}{R_0} \rho' , \end{aligned} \quad (18)$$

where

$$\mu = \frac{\omega_c^2}{\omega_r^2} - \frac{1}{2} , \quad (19)$$

$$\omega_r^2 = (1 - n) \omega_c^2 \quad (20)$$

is the radial betatron frequency-squared of electrons, $\gamma_\theta = (1 - \beta_\theta^2)^{-1/2}$ is the relativistic mass ratio associated with the axial electron velocity $\beta_\theta c$, A_r is the amplitude for radial betatron oscillations, $\delta P_\theta = P_\theta - P_0$, and $\tau = t' - t$. Within the context of Eq. (7), it is valid to approximate

$$\theta' = \omega_c - \mu \frac{\delta P_\theta}{\hat{\gamma} m R_0^2} \quad (21)$$

and to neglect the small oscillatory term $\omega_c \rho' / R_0$.

After a simple algebraic manipulation that makes use of Eq. (7), the perturbed distribution function in Eq. (4) is approximated by^{12,13}

$$\hat{f}_b = eI \left\{ \left[\left(1 - \frac{kV_z}{\omega} \right) R_0 \hat{E}_{\ell\theta}(R_0) + \frac{\ell V_z}{\omega} \hat{E}_{\ell z}(R_0) \right] \frac{\partial}{\partial P_\theta} f_b^0 \right. \\ \left. + \left[\frac{kV_\theta}{\omega} \hat{E}_{\ell\theta}(R_0) + \left(1 - \frac{\ell V_\theta}{\omega R_0} \right) \hat{E}_{\ell z}(R_0) \right] \frac{\partial}{\partial P_z} f_b^0 \right\}, \quad (22)$$

where the orbit integral I is defined by

$$I = \int_{-\infty}^0 d\tau \exp \left\{ i \left[\ell(\theta' - \theta) + k(z' - z) - \omega\tau \right] \right\} \\ = i \left(\omega - \ell\omega_c - \frac{kp_z}{\gamma m} + \ell\mu \frac{\delta P_\theta}{\gamma m R_0^2} \right)^{-1} \quad (23)$$

and use has been made of Eq. (8). Substituting Eq. (23) into Eq. (22) and carrying out a tedious but straightforward algebra, we obtain the perturbed distribution function

$$\hat{f}_b = i \frac{ec}{\gamma m R_0^2 \omega} \frac{\ell^2 \mu - k^2 R_0^2}{(\omega - \ell\omega_c - kV_z)^2} \left[\beta_\theta \hat{E}_{\ell\theta}(R_0) + \beta_z \hat{E}_{\ell z}(R_0) \right]. \quad (24)$$

Subsequently, integrals of the perturbed current density in the left-hand side of Eq. (14) are given by

$$\int_{R_1}^{R_2} dr \hat{J}_{\ell\theta}(r) = (\beta_\theta / \beta_z) \int_{R_1}^{R_2} dr \hat{J}_{\ell z}(r) \\ = -i \frac{\omega_c c \sigma}{2\pi\omega} \left[\beta_\theta \hat{E}_{\ell\theta}(R_0) + \beta_z \hat{E}_{\ell z}(R_0) \right], \quad (25)$$

where the effective susceptibility σ is defined by

$$\sigma(\omega, k) = \frac{\nu}{\gamma} \frac{c^2}{R_0^2} \frac{\ell^2 \mu - k^2 R_0^2}{(\omega - \ell \omega_c - k \beta_z c + i |k| \beta_z c \hat{\gamma} \Delta / \gamma_z^3)^2}, \quad (26)$$

and $\nu = N_b e^2 / mc^2$ is Budker's parameter.

Substituting Eq. (25) into Eq. (14), we obtain the matrix equation relating $\hat{E}_{\ell\theta}(R_0)$ and $\hat{E}_{\ell z}(R_0)$. The condition for a nontrivial solution to this matrix equation is that the determinant of the matrix vanishes. This gives the general dispersion relation

$$\frac{2}{\ell p^2 c^2} \left[\frac{\ell^2 \omega_c^2}{b_- + b_+} - \frac{(kc - \beta_z \omega)^2}{d_- + d_+} \right] \sigma + 1 = 0, \quad (27)$$

where use has been made of the approximation $\omega \approx \ell \omega_c + k \beta_z c$, which is consistent with Eq. (7). Defining the geometric factor $\Gamma(\omega, k)$

$$\Gamma(\omega, k) = \frac{\ell p^2 c^2}{2} \left[\frac{\ell^2 \omega_c^2}{b_- + b_+} - \frac{(kc - \beta_z \omega)^2}{d_- + d_+} \right]^{-1} \quad (28)$$

and substituting Eq. (26) into Eq. (27), the dispersion relation in Eq. (27) is expressed as

$$\Gamma(\omega, k) = - \frac{\nu}{\gamma} \frac{c^2}{R_0^2} \frac{\ell^2 \mu - k^2 R_0^2}{(\omega - \ell \omega_c - k \beta_z c + i |k| \beta_z c \hat{\gamma} \Delta / \gamma_z^3)^2} \quad (29)$$

which can be used to determine the complex eigenfrequency $\Omega = \omega - \ell \omega_c - k \beta_z c$ in terms of various physical parameters.

B. Geometric Factor $\Gamma(\omega, k)$

The evaluation of the wave admittances at the boundaries of the E-layer is required in order to complete the dispersion relation. To

make the theoretical analysis tractable, in the subsequent analysis, we concentrate the lowest modes of the electromagnetic waves inside the resonator where $R_a < r < R_c$. Moreover, the previous study^{14,15} have exhibited that the lowest modes in the resonator dominates the wave interaction. In this regard, for the transverse magnetic (TM) mode, we select (Appendix)

$$\hat{E}_z(r) = 0, R_a \leq r \leq R_c \quad (30)$$

which is lowest mode properly satisfying all the necessary boundary conditions. The Maxwell equations of the TM mode in the region $0 \leq r \leq R_a$ can be expressed as

$$\left(\frac{1}{r} \frac{\partial}{\partial r} r \frac{\partial}{\partial r} - \frac{l^2}{r^2} + p^2 \right) \hat{E}_{lz}(r) = 0 \quad (31)$$

except the inside of the E-layer (i.e., $R_1 < r < R_2$). Here $p^2 = \omega^2/c^2 - k^2$ is defined in Eq. (6). The physically acceptable solutions to Eq. (31) is given by

$$\hat{E}_{lz}(r) = \begin{cases} A J_l(pr) & , \quad 0 \leq r \leq R_1 & , \\ B [J_l(pr) - J_l(\eta)N_l(pr)/N_l(\eta)] & , \\ R_2 \leq r \leq R_a & , \end{cases} \quad (32)$$

where $J_l(x)$ and $N_l(x)$ are Bessel functions of the first and second kind, respectively, the parameter η is defined by

$$\eta^2 = (\omega^2/c^2 - k^2)R_a^2 & , \quad (33)$$

and A and B are constants. Substituting Eq. (32) into Eq. (11) and carrying out a straightforward algebra with a $\ll R_0$, we obtain a sum of the electric wave admittance

$$d_- + d_+ = \frac{2J_\ell(\eta)/\pi\ell}{J_\ell(\xi) [J_\ell(\xi)N_\ell(\eta) - J_\ell(\eta)N_\ell(\xi)]} \quad (34)$$

where $\xi = \eta R_0/R_a$.

Similarly, for the transverse electric (TE) mode, the sum of the magnetic wave admittances is expressed as (Appendix)

$$b_- + b_+ = \frac{2\ell G_\ell(\omega, k)/\pi\xi^2 J_\ell'(\xi)}{J_\ell'(\xi) + G_\ell(\omega, k)N_\ell'(\xi)} \quad (35)$$

where

$$G_\ell(\omega, k) = -\frac{J_\ell'(\eta)D(\omega, k)}{N_\ell'(\eta)F(\omega, k)}, \quad (36)$$

$$D(\omega, k) = \sum_{m=-\infty}^{\infty} \frac{J_n(\eta)}{J_n'(\eta)} \left(\frac{\sin n\alpha}{n\alpha} \right)^2 - \frac{\pi}{N\alpha} \frac{J_0(\eta)N_1(\zeta) - J_1(\zeta)N_0(\eta)}{J_1(\zeta)N_1(\eta) - J_1(\eta)N_1(\zeta)} \quad (37)$$

is the vacuum dispersion function,

$$F(\omega, k) = D(\omega, k) - \left[\frac{J_\ell(\eta)}{J_\ell'(\eta)} - \frac{N_\ell(\eta)}{N_\ell'(\eta)} \right] \left(\frac{\sin l\alpha}{l\alpha} \right)^2, \quad (38)$$

the integer n in Eq. (37) is defined by

$$n = s + mN \quad (39)$$

N is the number of the resonators, α is the half angle of the open spaces as shown in Fig. 1, s is an integer satisfying $0 \leq s \leq N - 1$, the prime(') denotes $(d/dx)J_\nu(x)$, and finally the parameter ζ is defined by

$$\zeta^2 = \eta^2 R_c^2 / R_a^2 = (\omega^2 / c^2 - k^2) R_c^2 . \quad (40)$$

For detailed information in deriving Eq. (35), we urge the reader to read the Appendix. Substituting Eqs. (34) and (35) into Eq. (28) completes the dispersion relation of the cusptron microwave tube.

III. VACUUM DISPERSION RELATION

In the absence of the beam [$v \rightarrow 0$ in Eq. (29)], the dispersion relation in Eq. (27) reduces to the TM dispersion relation

$$J_{\ell}(\eta) = 0 \quad (41)$$

and to the TE dispersion relation

$$G_{\ell}(\omega, k) = 0 \quad , \quad (42)$$

where use has been made of Eqs. (28), (34) and (35). The TM dispersion relation is equivalently expressed as

$$\frac{\omega^2}{c^2} - k^2 = \frac{\beta_{\ell n}^2}{R_a^2} \quad (43)$$

where $\beta_{\ell n}$ is the n th root of $J_{\ell}(\beta_{\ell n}) = 0$. Similarly, it is shown from Eq. (36) that the TE dispersion relation can be equivalently expressed as the ordinary TE mode

$$\frac{\omega^2}{c^2} - k^2 = \frac{\alpha_{\ell n}^2}{R_a^2} \quad (44)$$

and the magnetron TE mode

$$D(\omega, k) = \sum_{m=-\infty}^{\infty} \frac{J_n(\eta)}{J_n'(\eta)} \left(\frac{\sin n\alpha}{n\alpha} \right)^2 - \frac{\pi}{N\alpha} \frac{J_0(\eta)N_1(\zeta) - J_1(\zeta)N_0(\eta)}{J_1(\zeta)N_1(\eta) - J_1(\eta)N_1(\zeta)} = 0 \quad , \quad (45)$$

where α_{ln} is the n th root of $J'_l(\alpha_{ln}) = 0$. In Eq. (45), N is the number of resonators, α is the half angle of the open space in resonator, the integer n in Eq. (45) is defined by $n = s + mN$, $s = 0, 1, 2, \dots, N - 1$, and the parameter η and ζ are defined by $\eta^2 = \zeta^2 R_a^2 / R_c^2 = p^2 R_a^2 = (\omega^2/c^2 - k^2) R_a^2$ in Eq. (33).

In the remainder of this section, we investigate properties of the magnetron TE mode in Eq. (45) which relates the parameter η to the parameter ζ . In other words, the value of the parameter η is evaluated in term of $R_c/R_a = \zeta/\eta$. Once we determine value of the parameter η , the dispersion curve in (ω, k) parameter space is obtained from the relation

$$\omega^2/c^2 - k^2 = \eta^2/R_a^2 \quad (46)$$

Shown in Fig. 2 are plots of the parameters η (solid curves) and ζ (dashed curves) versus the radius ratio R_c/R_a for $N = 6$, $s = 0$, $\alpha = \pi/12$ and the three lowest radial modes. Several points are noteworthy in Fig. 2. First, as expected, value of the parameter η decreases monotonically as the ratio R_c/R_a increases. However, value of the parameter ζ stays relatively steady. Second, we note that values of parameters η and ζ at $R_c/R_a = 1$ are given by $\eta = \zeta = \alpha_{01} = 3.83$ for the lowest radial mode (the fundamental 2π mode), $\alpha_{02} = 7.02$ for the second and $\alpha_{61} = 7.50$ for the third mode. Finally, it is shown for the third radial mode that the value of the parameter η has a plateau for $1.2 < R_c/R_a < 1.4$.

Figure 3 is plots of the parameter η versus ratio R_c/R_a for $s = 0$, $\alpha = \pi/2N$, the lowest radial mode number, and several values of N . Remarkably, the value of the parameter η is relatively independent of

the number N for $N > 3$ and for the lowest radial mode number. On the other hand, for $N = 2$ and $R_c/R_a = 1$, the parameter η is given $\eta = \zeta = \alpha_{21} = 3.05$. Dependence of the parameter η on the integer s is presented in Fig. 4 where parameter η is plotted versus the ratio R_c/R_a for $N = 6$, $\alpha = \pi/12$, lowest radial mode number and different values of s . After a careful examination of Eq. (45), we note that the dispersion relation for $s = 1$ is identical to that for $s = N - 1$, and so on. In this regard, plots in Fig. 4 are presented only for the integer s satisfying $0 \leq s \leq N/2$. Obviously from Fig. 4, we conclude that the parameter η depends sensitively on the integer s . For $R_c/R_a = 1$, the value of the parameter η is given by $\eta = \alpha_{s1}$ for each s . Of course, the vacuum dispersion relation in Eq. (45) is also investigated for different values of the half angle α . Shown in Fig. 5 are plots of the parameter η versus the ratio R_c/R_a for $N = 8$, $s = 0$, lowest radial mode number and several values of α . Parameter η reduces with increasing value of the half angle α for the range $1 < R_c/R_a < 1.4$, which is a typical parameter range of present experiments.

IV. NEGATIVE-MASS INSTABILITY IN MAGNETRON-TYPE CONDUCTOR

In this section, we investigate stability properties of the negative-mass instability in a E-layer propagating through a magnetron-type conductor, by making use of the dispersion relation in Eq. (29). The growth rate and bandwidth of the negative-mass instability are directly related to the gain and bandwidth of the cusptron amplifier or oscillator. Making use of the fact that the "Doppler-shifted" eigenfrequency Ω in Eq. (7) is well removed from the electron cyclotron resonance, i.e., $|\Omega| \ll \omega_c$, and evaluating the function $\Gamma(\omega, k)$ at $k = k_b = (\omega - \ell\omega_c)/\beta_z c$ for the amplifier and at $\omega = \omega_b = \ell\omega_c + k\beta_z c$ for the oscillator, the dispersion relation in Eq. (29) can be approximated by

$$\left[\Gamma(\omega, k_b) - \frac{1}{\beta_z c} \left(\frac{\partial \Gamma}{\partial k} \right)_{k_b} \Omega \right] \left[\Omega + i \frac{|k_b| \beta_z c \hat{\gamma} \Delta}{\gamma_z^3} \right]^2$$

$$= - \frac{v_c^2}{2\hat{\gamma}R_0^2} (\ell^2 \mu - k_b^2 R_0^2)$$
(47)

for the amplifier and

$$\left[\Gamma(\omega_b, k) + \left(\frac{\partial \Gamma}{\partial \omega} \right)_{\omega_b} \Omega \right] \left[\Omega + i \frac{|k| \beta_z c \hat{\gamma} \Delta}{\gamma_z^3} \right]^2$$

$$= - \frac{v_c^2}{2\hat{\gamma}R_0^2} (\ell^2 \mu - k^2 R_0^2)$$
(48)

for the oscillator. In the remainder of this section, the growth rate $\Omega_i = \text{Im}\Omega$ and the Doppler-shifted real oscillation frequency $\Omega_r = \text{Re}\Omega$ are numerically calculated from Eq. (47) for the amplifier and from Eq. (48) for the oscillator. Numerical calculation is carried out for the nonrelativistic electron beam parameters $v = 0.002$, $\Delta = 0.04$, $\beta_\theta = 0.4$ and $\beta_z = 0.2$ corresponding to $\hat{\gamma} = 1.118$. For a relativistic beam, $\beta_\theta = 0.96$ and $\beta_z = 0.2$ corresponding to $\hat{\gamma} = 5.1$.

To the lowest order, the eigenfrequency ω and axial wavenumber k are obtained from the simultaneous solution of the vacuum waveguide mode dispersion relation,

$$\frac{\omega^2}{c^2} - k^2 = \frac{n^2}{R_a^2} \quad , \quad (49)$$

and the condition for cyclotron resonance

$$\omega = l\omega_c + k\beta_z c. \quad (50)$$

Moreover, to maximize the growth rate and efficiency of microwave generation and amplification, it is required that the group velocity of the vacuum waveguide mode in Eq. (49) be approximately equal to the beam velocity, i.e.,

$$v_g = d\omega/dk = kc^2/\omega = \beta_z c \quad . \quad (51)$$

Solving Eqs. (50) and (51) for the characteristic frequency and axial wavenumber $(\omega, k) = (\omega_0, k_0)$, we find (Fig. 6)

$$\omega_0 = l\omega_c \gamma_z^2 \quad , \quad k_0 = l\omega_c \beta_z \gamma_z^2 / c \quad . \quad (52)$$

For maximum growth, it is also required that (ω_0, k_0) solve Eq. (49) in leading order. Therefore, for maximum efficiency, we find that R_a should satisfy

$$R_a = \eta c / \ell \omega_c \gamma_z \quad (53)$$

Under the grazing condition in Eq. (53), the cyclotron resonance mode in Eq. (50) is a tangential line of the vacuum waveguide mode in Eq. (49), as shown in Fig. 6. Noting $\beta_\theta = R_0 \omega_c / c$, it is found from Eq. (53) that the beam radius is determined from

$$R_0 / R_a = \beta_\theta c / R_a \omega_c = \ell \beta_\theta \gamma_z / \eta \quad (54)$$

and that the parameter η should satisfy the inequality

$$\eta / \ell \gamma_z > \beta_\theta \quad (55)$$

for a physically acceptable cusptron microwave tube.

A. Nonrelativistic Cusptron Amplifier

In this section, we summarize results of numerical calculation from Eq. (47) for the amplifier in a nonrelativistic electron beam ($\beta_0 = 0.4$) propagating through a uniform applied magnetic field with the field index $n = 0$. Shown in Fig. 7 is a plot of the geometric factor $\Gamma(\omega, k_b)$ versus normalized frequency ω / ω_c in Eq. (28) for $N = 6$, $\ell = 6$, $s = 0$, $\alpha = \pi/12$, $R_c / R_a = 1.4$ and $R_a \omega_c / c = 0.4433$ corresponding to the grazing condition in Eq. (53) for the parameter $\eta = 2.715$ in Fig. 2. Here the axial wavenumber k is substituted by $k_b = (\omega - \ell \omega_c) / \beta_z c$ consistent with the dispersion relation in Eq. (47) for amplifiers. As

expected from the condition $R_a \omega_c / c = 0.4433$, the curve of the geometric factor Γ grazes the horizontal line. Values of the geometric factor Γ are very close to zero in a considerable range (i.e., $6 < \omega / \omega_c < 6.5$ in Fig. 7) of ω space, thereby exhibiting possibility of broad unstable frequency range.

Figure 8 shows plots of (a) normalized growth rate Ω_1 / ω_c and (b) Doppler-shifted real frequency Ω_r / ω_c versus ω / ω_c obtained from Eq. (47) for the electron beam parameters $\nu = 0.002$, $\Delta = 0.04$, $\beta_\theta = 0.4$, $\beta_z = 0.2$, the field index $n = 0$ and the grazing conditions (i.e., $R_a \omega_c / c = 0.4433$ for $R_c / R_a = 1.4$, 0.4934 for $R_c / R_a = 1.3$, 0.5453 for $R_c / R_a = 1.2$, 0.5905 for $R_c / R_a = 1.1$ and 0.6257 for $R_c / R_a = 1$), corresponding to fundamental 2π mode, and parameters otherwise identical to Fig. 7. For each value of R_c / R_a , the growth rate curve consists of two parts; solid line corresponding to relatively large Doppler-shifted real frequency and dashed line corresponding to very small Doppler-shifted real frequency [Figs. 8(a) and (b)]. The efficiency of microwave tube is directly proportional to the Doppler-shifted real frequency.¹⁶ In this regard, even though instability of the dashed curve exhibits large growth rate, there is no significant amplification in this frequency range corresponding to small Doppler-shifted real frequency. Obviously from Fig. 8(a), the amplification growth rate [solid curve in Fig. 8(a)] reduces as R_c / R_a approaches to unity. In particular, for $R_c / R_a = 1$, the amplification growth rate vanishes, thereby smoothly connecting two dashed curves in Fig. 8(a). In this case ($R_c / R_a = 1$), the Doppler-shifted real frequency Ω_r / ω_c is less than 0.003. We also

note from Figure 8(a) that the maximum growth rate of the cusptron is more than five times that for conventional gyrotron amplifier [Curve for $R_c/R_a = 1.4$ in Figure 8(a)]. Also the Doppler-shifted real frequency for $R_c/R_a = 1.4$ in Figure 8(b) exhibits a strong possibility of very high efficiency in microwave amplification.

Numerical investigation of Equation (47) has been also carried out for a broad range of physical parameters s , ℓ , α , N and various radial mode number. From this numerical calculation, we make several conclusions. First, under the grazing condition $R_a = nc/N\omega_c \gamma_z$ corresponding to $\ell = N$, there is no amplification growth rate of instability for perturbations with $\ell \neq N$ azimuthal harmonic number. Second, optimizing value of the parameter $R_a \omega_c / c$ according to Equation (53), the $\ell \neq N$ perturbations also have substantial amount of the amplification growth rate with relatively large Doppler-shifted real frequency. However, comparing with Figure 8, we conclude that the amplification growth rate of the $\ell = N$ perturbation is largest and is most effective means of the microwave amplification. Third, after optimizing the parameter $R_a \omega_c / c$ according to Equation (53), the $s = 0$ perturbation is the best in the microwave amplification. Fourth, it is found that the lowest radial mode perturbation is dominant unstable mode. Fifth, we also found from the numerical calculation that after optimizing $R_a \omega_c / c$, the growth rate and Doppler-shifted real frequency are almost independent of α in the range $\pi/4N < \alpha < \pi/2N$ for $s = 0$, $\ell = N$ and the lowest radial mode number. However, increasing α from $\pi/2N$ to π/N reduces drastically the growth rate and Doppler-shifted real frequency. Finally, stability properties have been investigated

also for $N = 4$ and parameters otherwise identical to Figure 8. It has been shown from numerical calculation that the maximum growth rate and Doppler-shifted real frequency of $N = 4$ are comparable to those of $N = 6$ case. However, the optimum value of the growth rate and real frequency occurs at $R_c/R_a = 1.8$ and $R_a\omega/c = 0.4494$. After consideration of all of these properties, we conclude for the nonrelativistic electron beam with $\beta_\theta = 0.4$ that the optimum physical parameters for microwave amplification are $N = 6$, $\ell = 6$, $s = 0$, $\alpha = \pi/12$, $R_c/R_a = 1.4$ and $R_a\omega/c = 0.4433$.

B. Effect of Non-Zero Field Index

As shown in Equations (47) and (48), the coupling coefficient is directly proportional to the parameter

$$\mu = \frac{1}{1-n} - \frac{1}{\gamma_\theta^2} = \beta_\theta^2 + \frac{n}{1-n}, \quad (56)$$

where n is the field index defined in Equation (16). Evidently from Equation (56), for nonrelativistic beam with $\beta_\theta^2 \ll 1$, small increase of the field index from zero makes a big difference in the coupling coefficient, thereby enhancing the gain and efficiency of the microwave amplification. Shown in Figure 9 is plots of (a) normalized growth rate Ω_1/ω_c and (b) Doppler-shifted real oscillation frequency Ω_r/ω_c obtained from Equation (47) for $R_c/R_a = 1.4$, $R_a\omega/c = 0.4433$, several different values of the field index n , and parameters otherwise identical to Figure 8. Obviously, the growth rate and real frequency increase substantially by increasing the field index from zero to a small positive value. However, since the applied magnetic field is not anymore uniform along the axial direction for non-zero field index,

tapering of the conducting wall radius R_a is required in order to match the grazing condition in Equation (53) (e.g., $R_a \omega_c / c = 0.4433$ in Figure 9).

C. Nonrelativistic Cusptron Oscillator

The growth rate and Doppler-shifted real oscillation frequency are numerically obtained from Equation (48) for the oscillations in a nonrelativistic electron beam. Figure 10 is plots of (a) normalized growth rate and (b) Doppler-shifted real frequency versus normalized axial wavenumber kc/ω_c obtained from Equation (48) for the parameters identical to Figure 8. Normalized lowest order eigenfrequency $\omega_b/\omega_c = \ell + k\beta_z c/\omega_c$ is also shown in the horizontal scale in Figure 10. Comparing Figure 10(a) with Figure 8(a), we note that unstable range in frequency space for the oscillation is broader than that for the amplifier. Perturbations in the amplifier are unstable only for the positive k-space. Moreover, the real frequency in the oscillator is considerably different from that in the amplifier [Figures 8(b) and 10(b)].

D. Relativistic Cusptron Amplifier

Preliminary investigation of Equation (47) has been carried out for the amplifiers in a relativistic electron beam with $\beta_\theta = 0.96$ and $\beta_z = 0.2$. After a careful examination of Equation (55) and Figure 2, we note for the relativistic electron beam ($\beta_\theta \rightarrow 1$) that the first available coupling occurs at the third lowest radial mode number where the parameter η is larger than N for a reasonable range of R_c/R_a . Figure 11 shows plots of (a) normalized growth rate Ω_1/ω_c and (b) Doppler-shifted real frequency Ω_r/ω_c versus ω/ω_c for $\beta_\theta = 0.96$, the grazing conditions ($R_a \omega_c / c = 1.1101$ for $R_c/R_a = 1.5$, 1.1679 for $R_c/R_a = 1.25$ and 1.2249 for $R_c/R_a = 1$), and parameters otherwise

identical to Figure 8. Contrary to a nonrelativistic cusptron amplifiers (in Figure 8), the growth rate and bandwidth of instability in Figure 11 increase drastically as R_c/R_a approaches to unity. However, for $R_c/R_a = 1.5$ and $R_a \omega_c/c = 1.1101$, the Doppler-shifted real frequency of perturbations with $\ell \neq N$ azimuthal mode number vanishes, while the $\ell = N$ perturbation has considerably large Doppler-shifted real frequency. In this regard, by selecting $R_c/R_a = 1.5$ and $R_a \omega_c/c = 1.1101$, microwaves with $\ell = N$ mode perturbations are dominantly amplified, thereby optimizing the microwave power output for radiation with frequency $\omega = \ell \omega_c$. On the other hand, for $R_c/R_a = 1$, various other modes compete with the $\ell = N$ mode, leading to multi-mode amplification. Therefore, even though the growth rate for $R_c/R_a = 1.5$ is less than that for $R_c/R_a = 1$, geometric configuration with $R_c/R_a = 1.5$ is more effective to amplify microwaves. Numerical investigation of Equation (47) for $N = 12$ and $N = 24$ also exhibits very similar properties.

After a careful examination of the geometric factor $\Gamma(\omega, k)$ for a broad range of various physical parameters, it can be found

$$\begin{aligned} \Gamma(\omega, k_b) &\approx 0, \\ [\partial \Gamma(\omega, k) / \partial k]_{k = k_b} &= 0, \end{aligned} \quad (57)$$

for particular values of $R_a \omega_c/c$ and frequency ω . In this case, in order to correctly evaluate the gain of the cusptron, we approximate Equation (29) by

$$\begin{aligned} &\left[\Gamma(\omega, k_b) - \frac{1}{\beta_z c} \left(\frac{\partial}{\partial k} \Gamma \right)_{k_b} \Omega + \frac{1}{2\beta_z^2 c^2} \left(\frac{\partial^2}{\partial k^2} \Gamma \right)_{k_b} \Omega^2 \right] \\ &\times \left[\Omega + i \frac{|k_b| \beta_z c \tilde{\gamma} \Delta}{\gamma_z^3} \right]^2 = - \frac{v c^2}{2\tilde{\gamma} R_0^2} \left(\ell^2 \mu - k_b^2 R_0^2 \right). \end{aligned} \quad (58)$$

Of course, the dispersion relation in Equation (47) is used to obtain the gain for a broad range of physical parameters except ω satisfying Equation (57). Obviously, Equation (47) fails to estimate the gain for this frequency range. We therefore make use of Equation (58) to obtain the gain at the frequency satisfying Equation (57). We also emphasize the reader that the gain of the cusptron amplifier at the frequency ω corresponding to Equation (57) is significantly greater than that at other frequencies.

In order to illustrate a high gain cusptron amplification, shown in Figure 12 are plot of the normalized growth rate Ω_1/ω_c versus ω/ω_c obtained from Equations (47) and (58) for $\beta_\theta = 0.96$, $N = 24$, $l = 25$, $R_c/R_a = 1.1$, $R_a\omega_c/c = 1.069$ and parameters otherwise identical to Figure 8. The dashed curves in Figure 12 are plot of the gain obtained from Equation (47) in the frequency range satisfying Equation (57). Obviously Equation (47) fails in this frequency range. However, Equation (58) correctly evaluates the growth rate in this region. As expected, the maximum gain in Figure 12 is considerably enhanced in comparison with that of ordinary cusptron amplifier (Figures 8 and 11). However, the Doppler-shifted real frequency in this frequency range is comparable or smaller than that for other frequency ranges. Other detailed properties of the relativistic cusptron amplifiers and oscillators are currently under investigation by authors for a broad range of physical parameters and will be published elsewhere.

V. CONCLUSIONS

In this paper, we have investigated the negative-mass stability properties of an E-layer propagating through a magnetron-type conductor, in connection with application on the cusptron amplifier and oscillator. Stability analysis has been carried out within the framework of the linearized Vlasov-Maxwell equations, assuming that the E-layer is thin and in a fast rotational equilibrium. The formal dispersion relation of the negative-mass instability was obtained in Section V, including the important influence of the magnetron-type conductor which has periodic resonators. Properties of the vacuum waveguide mode in a magnetron-type conductor have been briefly investigated in Section III, without including the influence of beam electrons. Making use of the vacuum dispersion relation, the cut-off frequency $\omega_{ct} = \eta c/R_a$ has been calculated in terms of the radius ratio R_c/R_a . For the number N of the resonator more than three, it has been shown for the fundamental 2π mode with $s = 0$ that $\omega R_a/c = \alpha_{01} = 3.83$ when $R_c/R_a = 1$. In Section IV, the negative-mass stability properties of an E-layer were numerically investigated, including the important influence of the magnetron-type conductor. Several points are noteworthy from this numerical calculation for a nonrelativistic cusptron amplifier or oscillator. First, optimum coupling occurs between the beam and the fundamental 2π modes. Utilizing the fundamental 2π mode, it was shown that for typical present experimental beam parameters, gain and efficiency of the cusptron can be more than five times those of the gyrotron. Second, for the applied magnetic field satisfying the grazing condition $R_a \omega/c = \eta/NY_z$ of the $\ell = N$ perturbations, other azimuthal perturbations with $\ell \neq N$

are suppressed. Therefore, under this grazing condition, the $l = N$ mode perturbation is the dominant unstable mode, optimizing the microwave power output for radiation with frequency $\omega = l\omega_c$. In this regard, even for relatively small applied field, high frequency microwaves can be amplified by making use of the cusptron with $N \geq 2$. Finally, the growth rate and Doppler-shifted real oscillation frequency are substantially increased by changing the applied field index from zero to a small positive value. Preliminary investigation of a relativistic cusptron amplifier has been carried out, and it has been shown that the stability trend of the relativistic cusptron is similar to the nonrelativistic case.

VI. ACKNOWLEDGEMENTS

This research was supported by the Independent Research Fund at the Naval Surface Weapons Center.

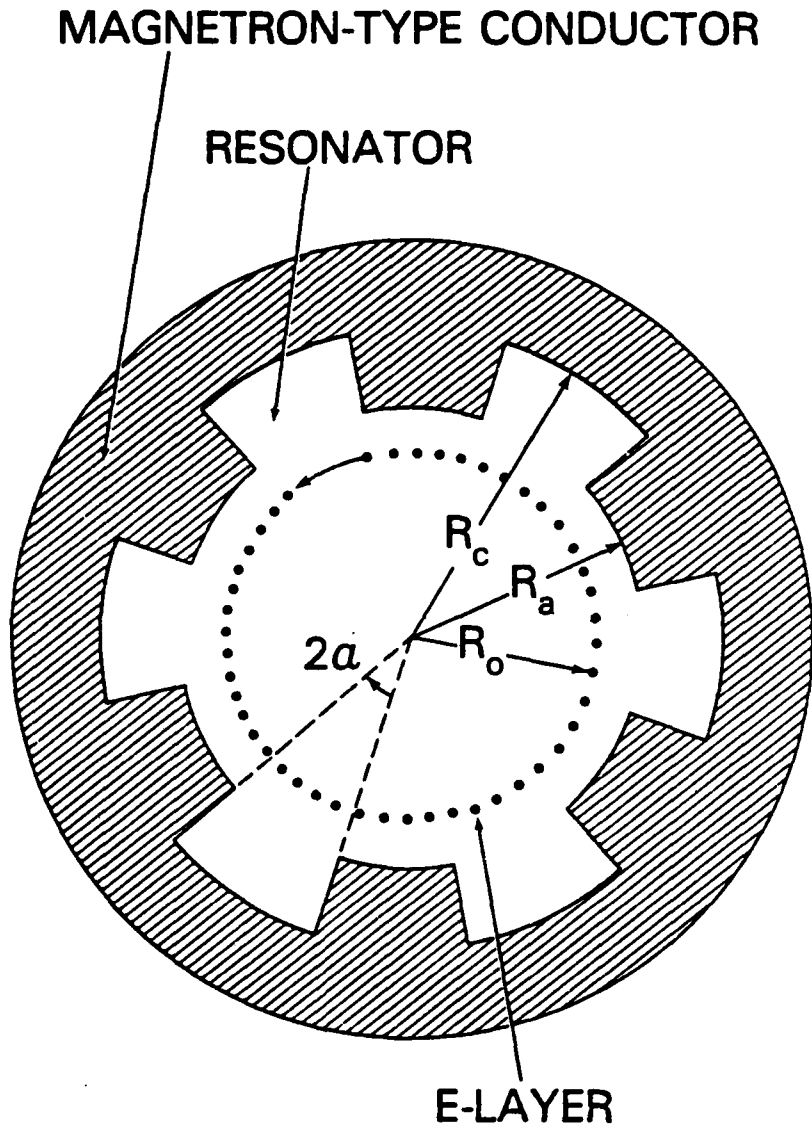


FIGURE 1. CROSS SECTIONAL VIEW OF CUSPTRON

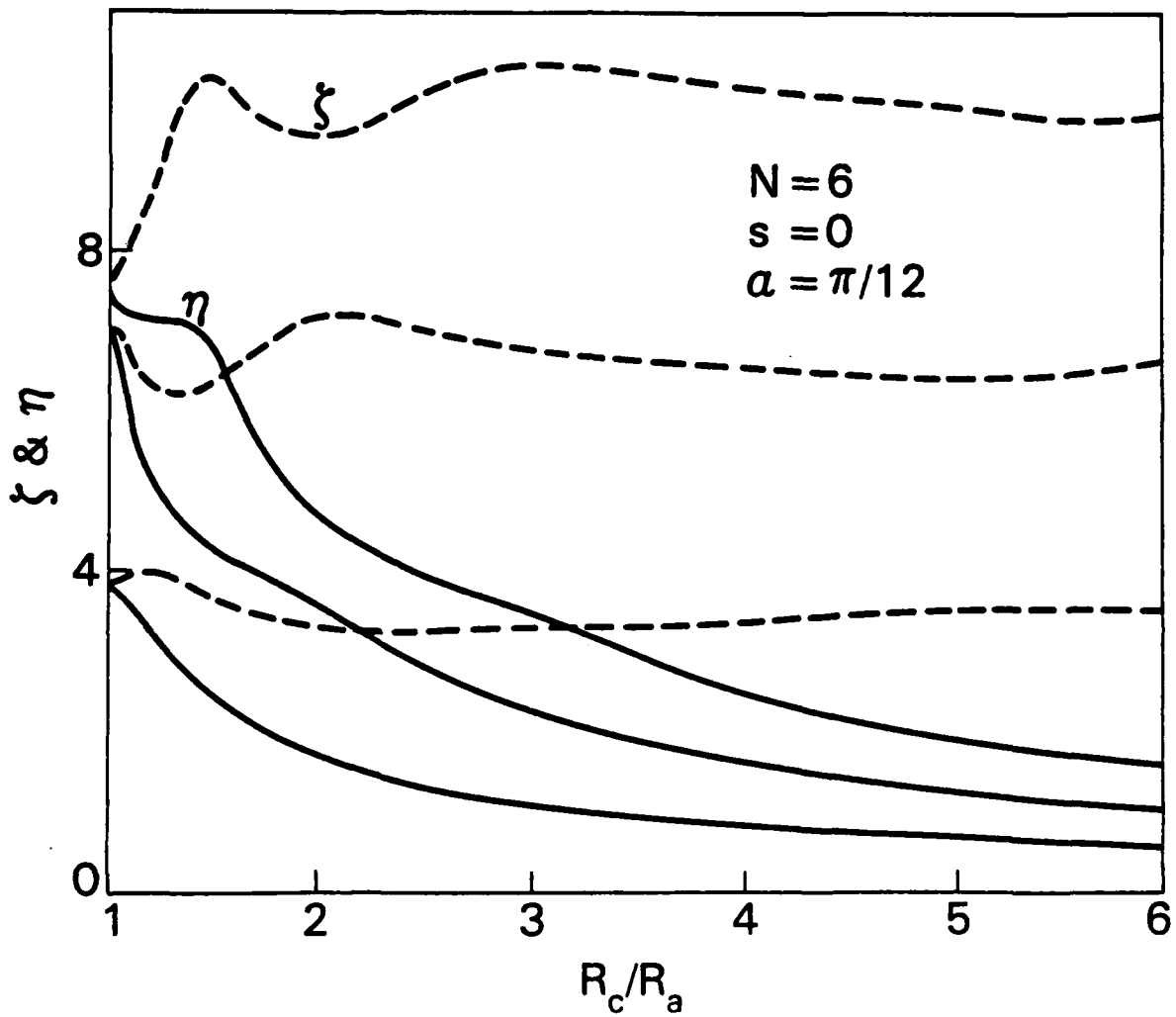


FIGURE 2. PLOTS OF THE PARAMETERS η (SOLID CURVES) AND ζ (DASHED CURVES) VERSUS RATIO R_c/R_a [OBTAINED FROM EQ. (45)] FOR $N = 6$, $s = 0$, $a = \pi/12$ AND THREE LOWEST RADIAL MODES

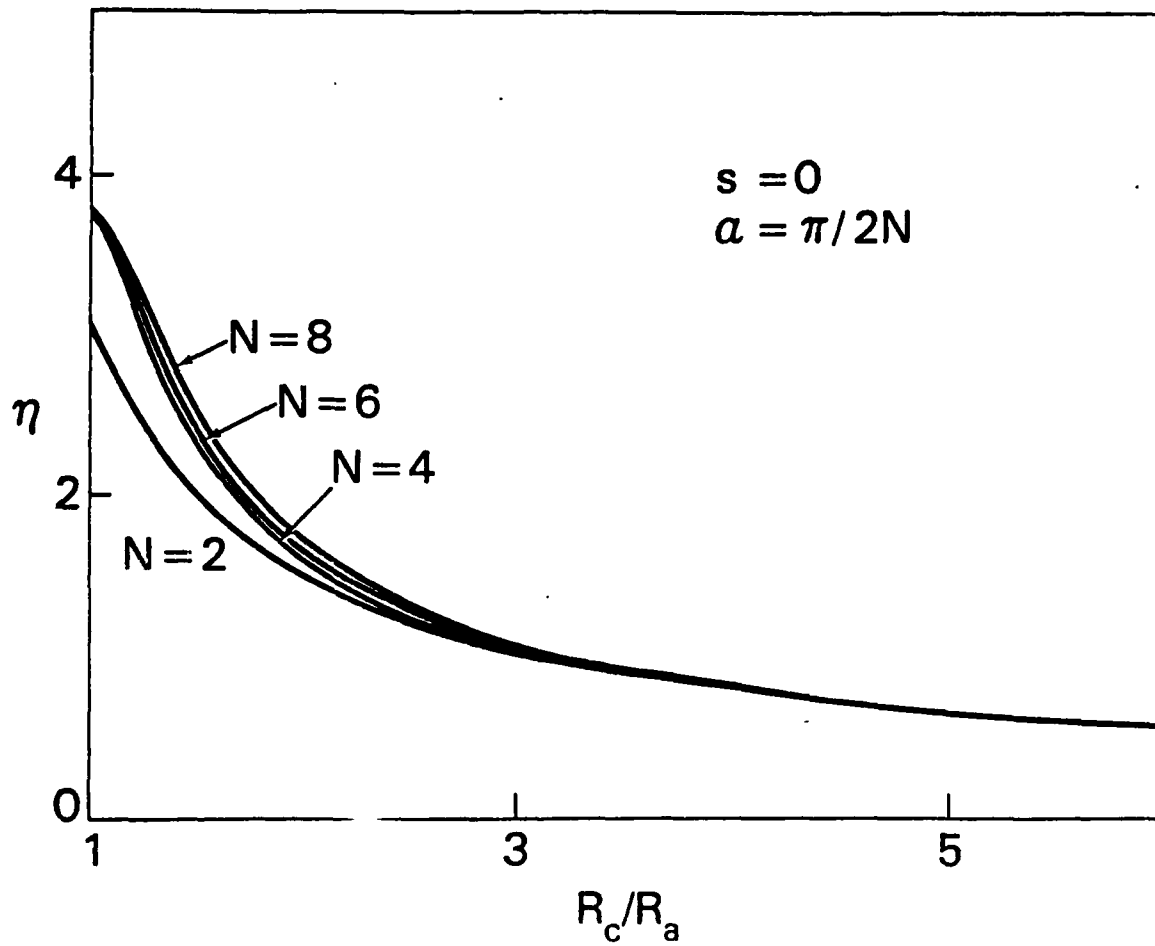


FIGURE 3. PLOTS OF PARAMETER η VERSUS RATIO R_c/R_a OBTAINED FROM EQ. (45) FOR $s = 0$, $\alpha = \pi/2N$, LOWEST RADIAL MODE NUMBER, AND SEVERAL VALUES OF N

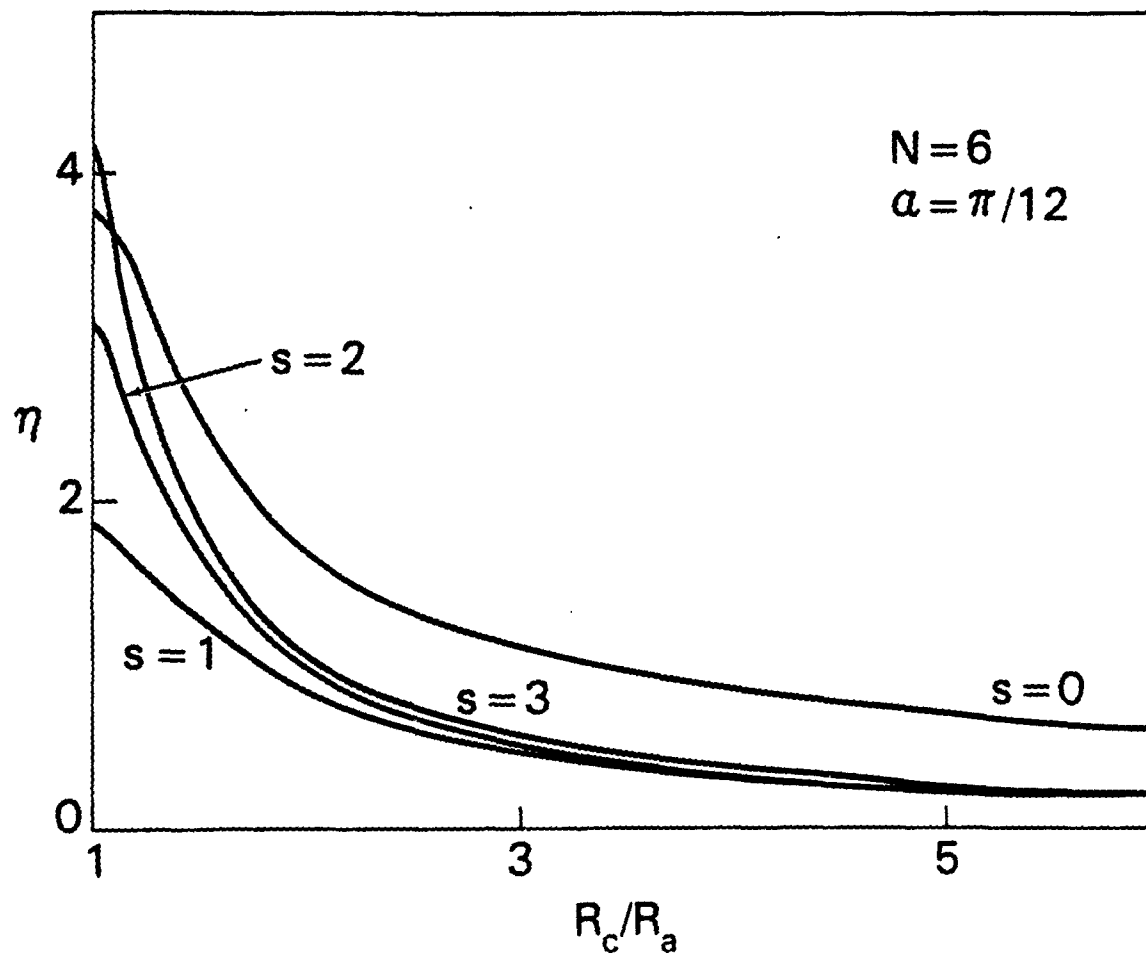


FIGURE 4. PLOTS OF PARAMETER η VERSUS RATIO R_c/R_a OBTAINED FROM EQ. (45) FOR $N = 6$, $\alpha = \pi/12$, LOWEST RADIAL MODE NUMBER AND DIFFERENT VALUES OF s

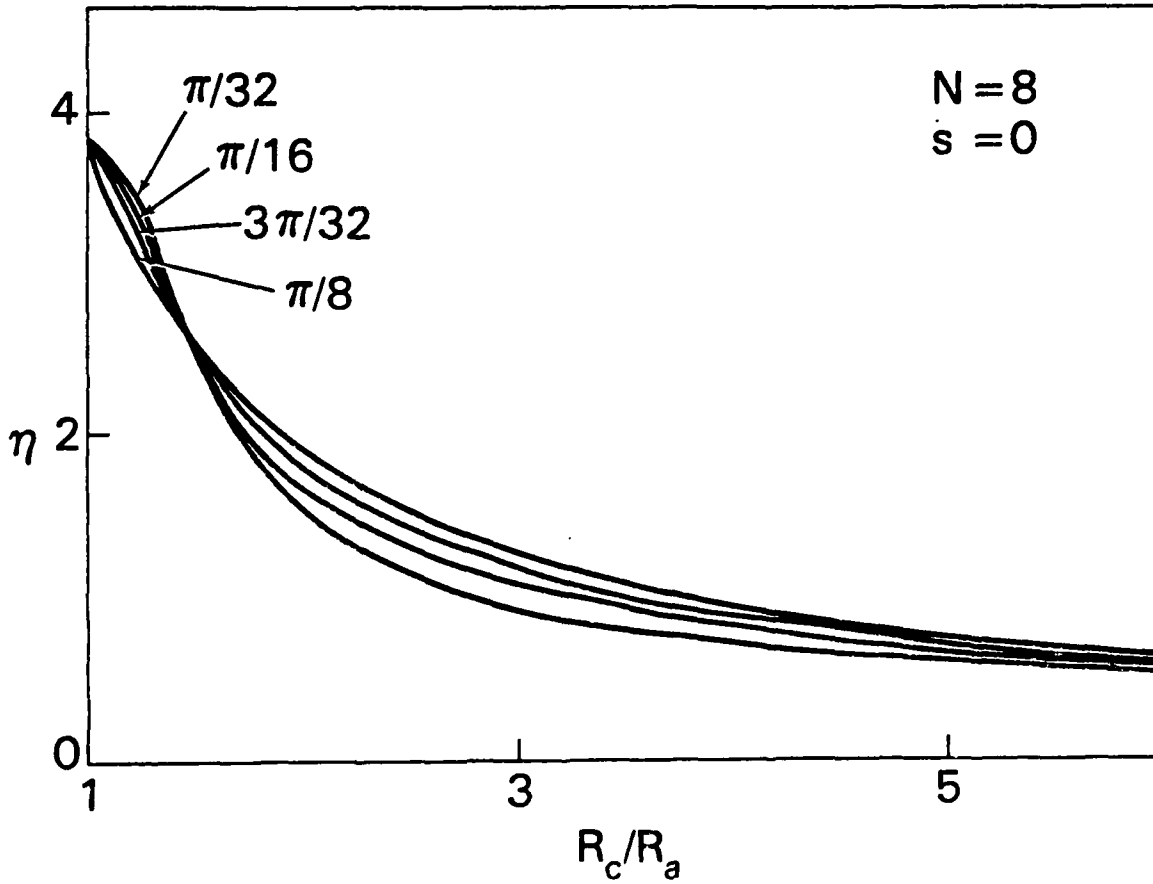


FIGURE 5. PLOTS OF PARAMETER η VERSUS RATIO R_c/R_a OBTAINED FROM EQ. (45) FOR $N = 8$, $s = 0$, LOWEST RADIAL MODE NUMBER AND SEVERAL VALUES OF α

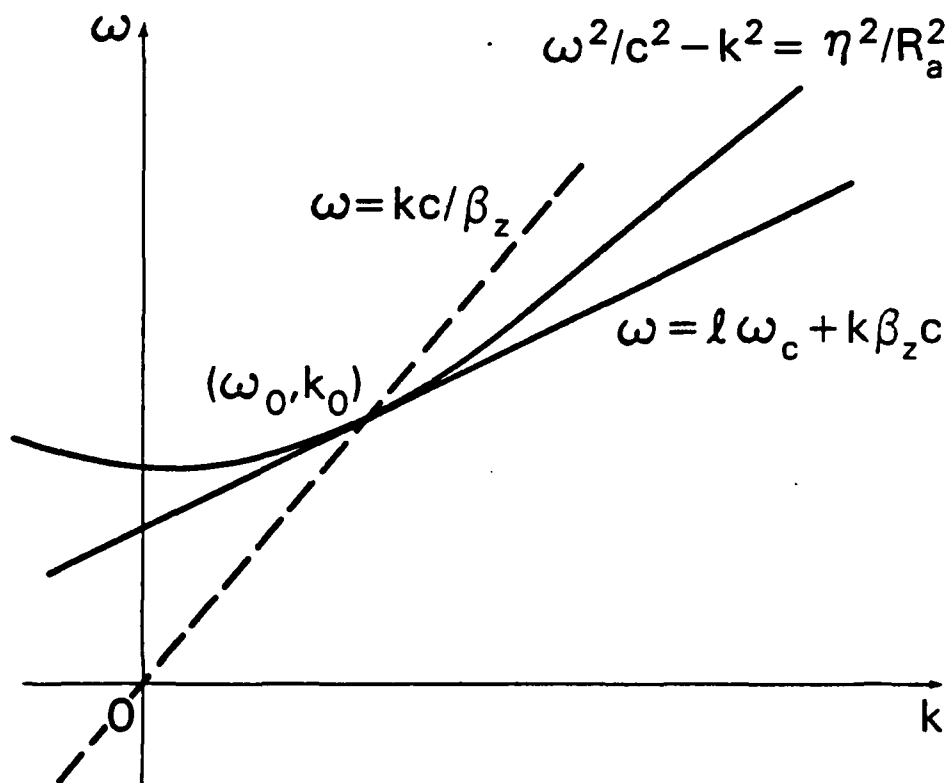


FIGURE 6. THE STRAIGHT LINES $\omega = k\beta_z c + l\omega_c$ AND $\omega = kc/\beta_z$ INTERSECT AT $(\omega_0, k_0) = (l\omega_c \gamma_z^2, l\omega_c \beta_z \gamma_z^2/c)$. THE VACUUM WAVEGUIDE MODE $\omega = (k^2 c^2 + \eta^2 c^2/R_a^2)^{1/2}$ PASSES THROUGH (ω_0, k_0) PROVIDED $R_a \omega_c/c = \eta/l\gamma_z$

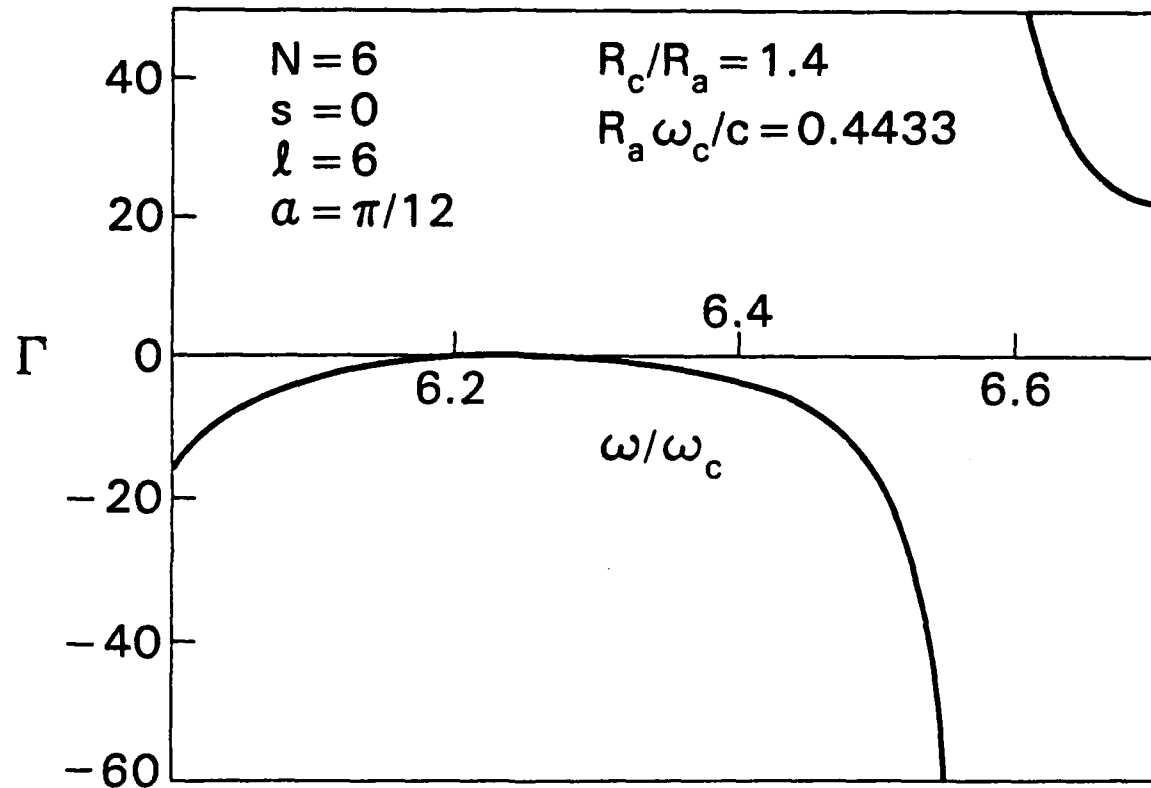


FIGURE 7. PLOT OF THE GEOMETRIC FACTOR $\Gamma(\omega, k_b)$ VERSUS NORMALIZED FREQUENCY ω/ω_c IN EQ. (28) FOR $N = 6$, $l = 6$, $s = 0$, $a = \pi/12$, $R_c/R_a = 1.4$ AND $R_a \omega_c / c = 0.4433$ CORRESPONDING TO THE GRAZING CONDITION FOR $\hat{r}_2 = 0.2$

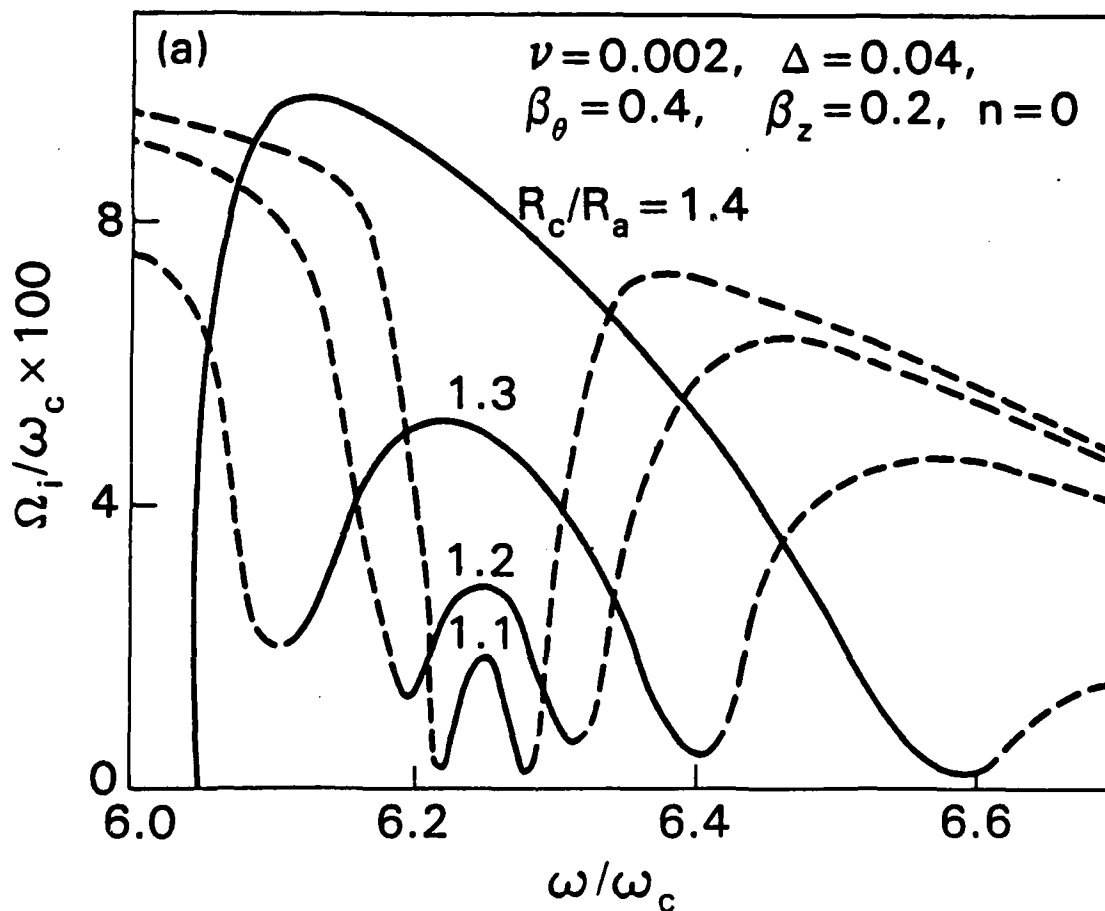


FIGURE 8. PLOTS OF (a) NORMALIZED GROWTH RATE Ω_i/ω_c AND DOPPLER-SHIFTED REAL OSCILLATION FREQUENCY Ω_r/ω_c VERSUS ω/ω_c OBTAINED FROM EQ. (47) FOR ELECTRON BEAM PARAMETERS $\nu = 0.002, \Delta = 0.04, \beta_\theta = 0.4, \beta_z = 0.2$, FIELD INDEX $n = 0$ AND THE GRAZING CONDITIONS CORRESPONDING TO EQ. (53), AND PARAMETERS OTHERWISE IDENTICAL TO FIGURE 7

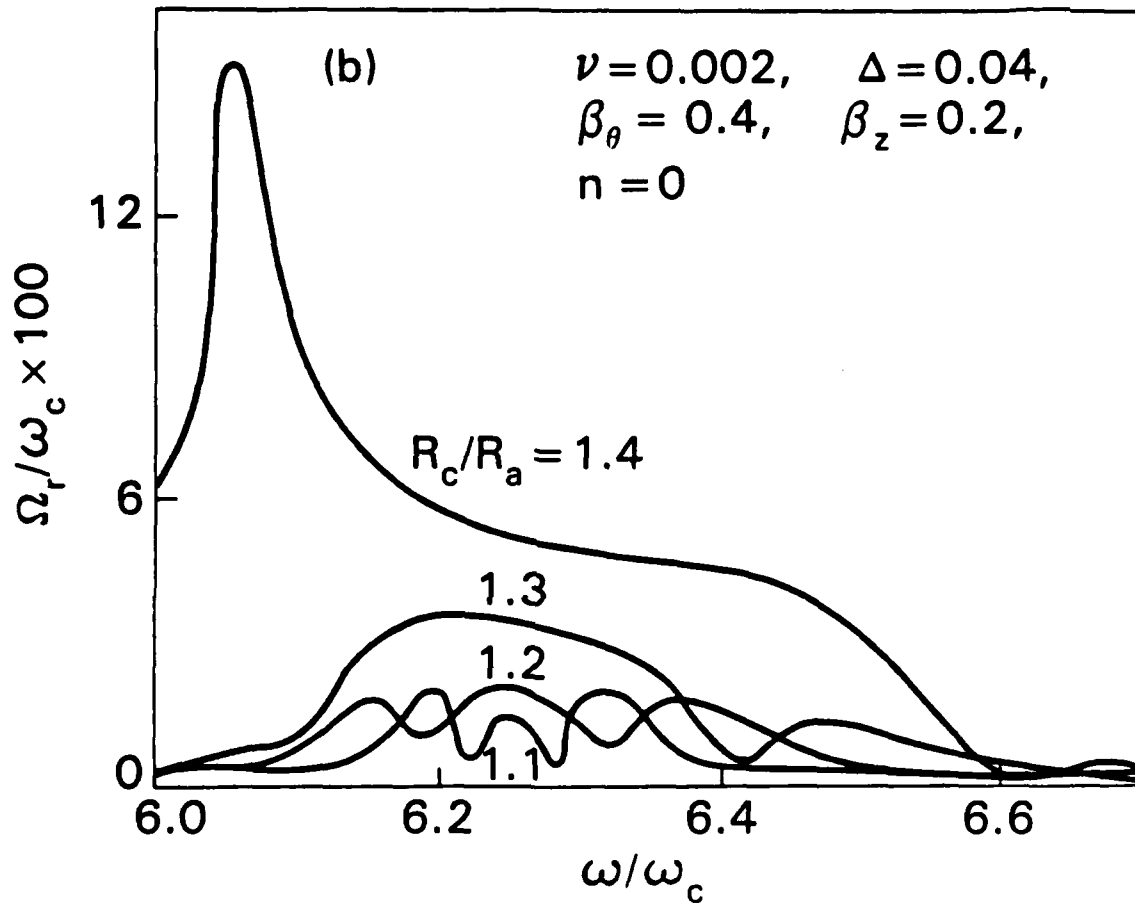


FIGURE 8. (CONTINUED)

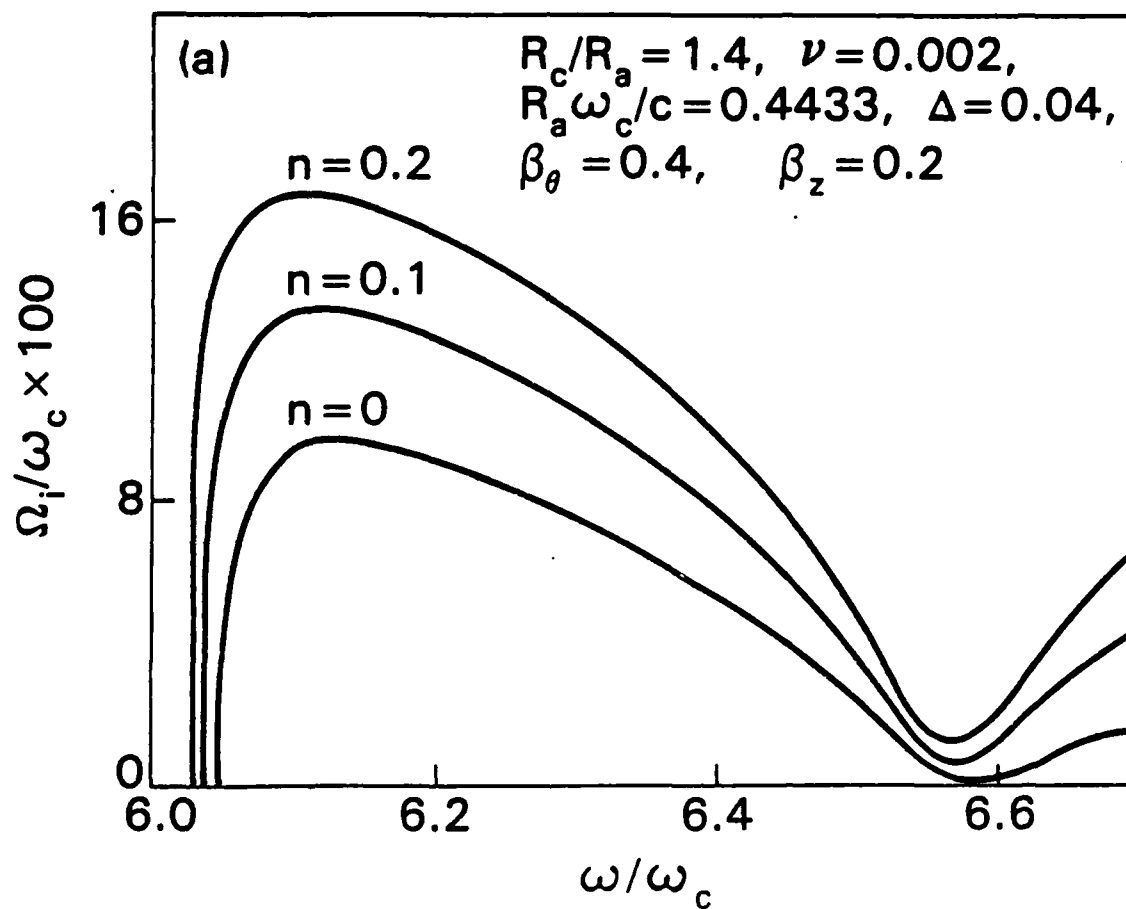


FIGURE 9. PLOTS OF (a) NORMALIZED GROWTH RATE Ω_i/ω_c AND (b) DOPPLER-SHIFTED REAL OSCILLATION FREQUENCY Ω_r/ω_c VERSUS ω/ω_c OBTAINED FROM EQ. (47) FOR $R_c/R_a = 1.4, R_a \omega_c/c = 0.4433$, SEVERAL DIFFERENT VALUES OF THE FIELD INDEX n , AND PARAMETERS OTHERWISE IDENTICAL TO FIGURE 8

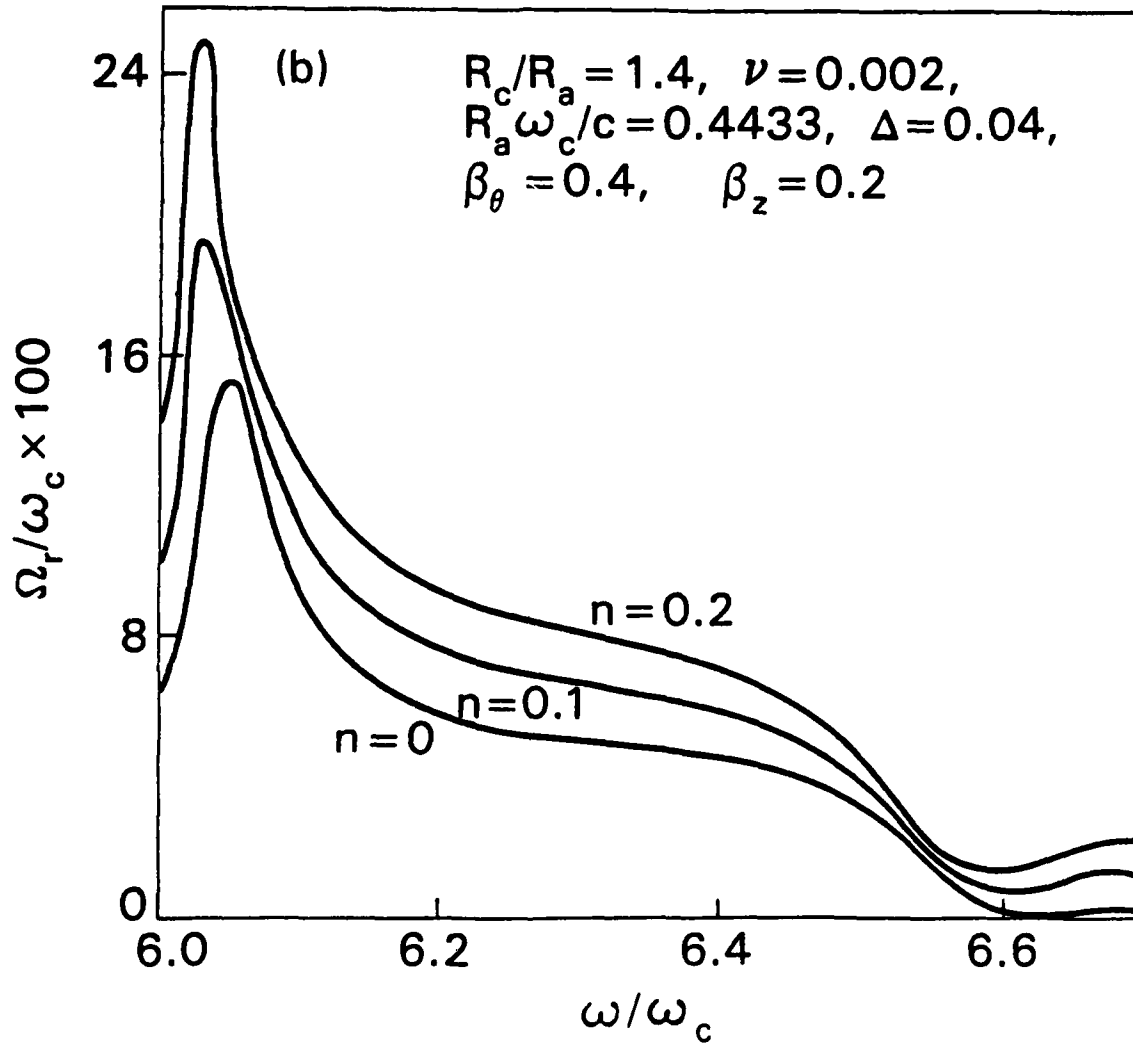


FIGURE 9. (CONTINUED)

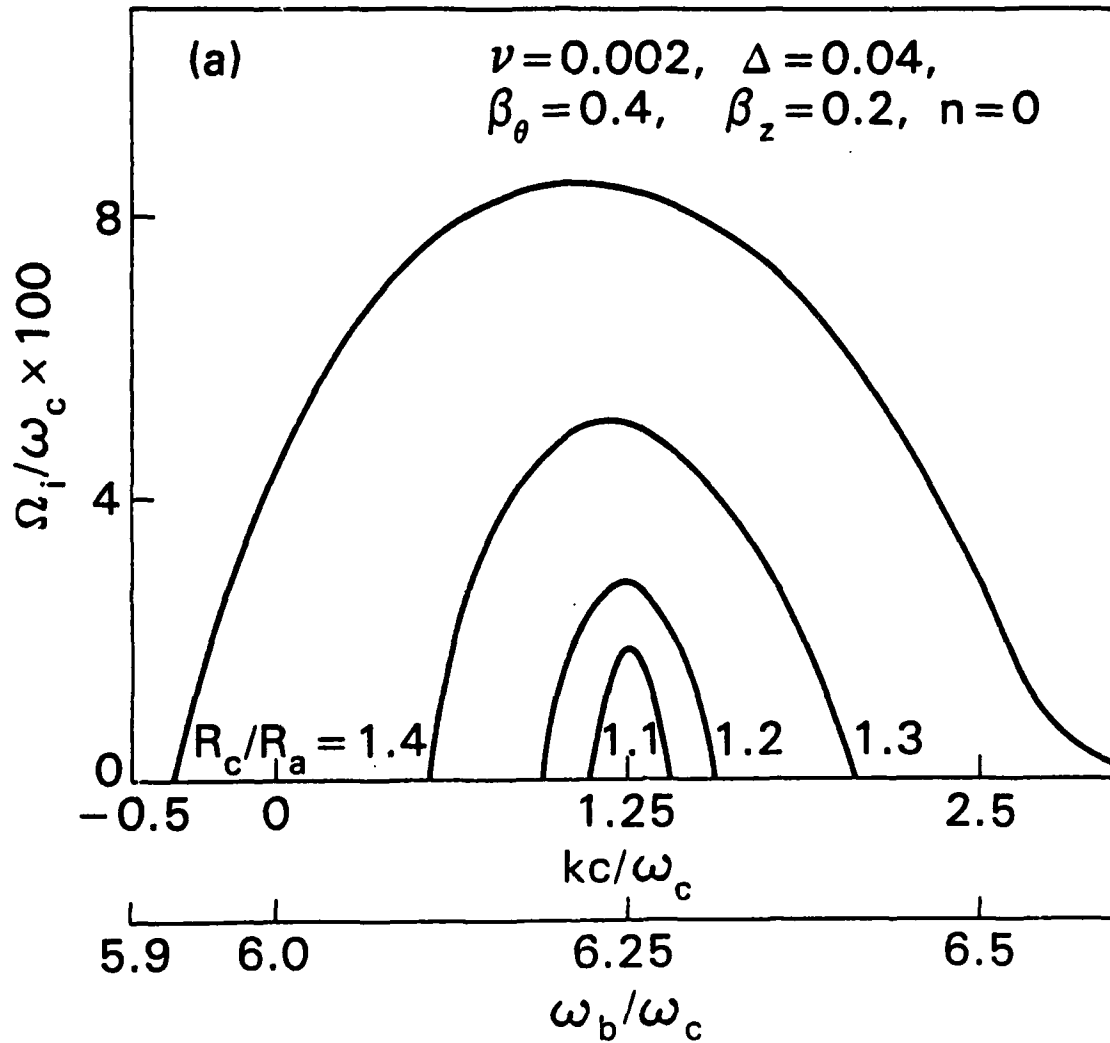


FIGURE 10. PLOTS OF (a) NORMALIZED GROWTH RATE Ω_i/ω_c AND (b) DOPPLER-SHIFTED REAL FREQUENCY Ω_r/ω_c VERSUS NORMALIZED AXIAL WAVE NUMBER kc/ω_c OBTAINED FROM EQ. (48) FOR THE PARAMETERS IDENTICAL TO FIGURE 8

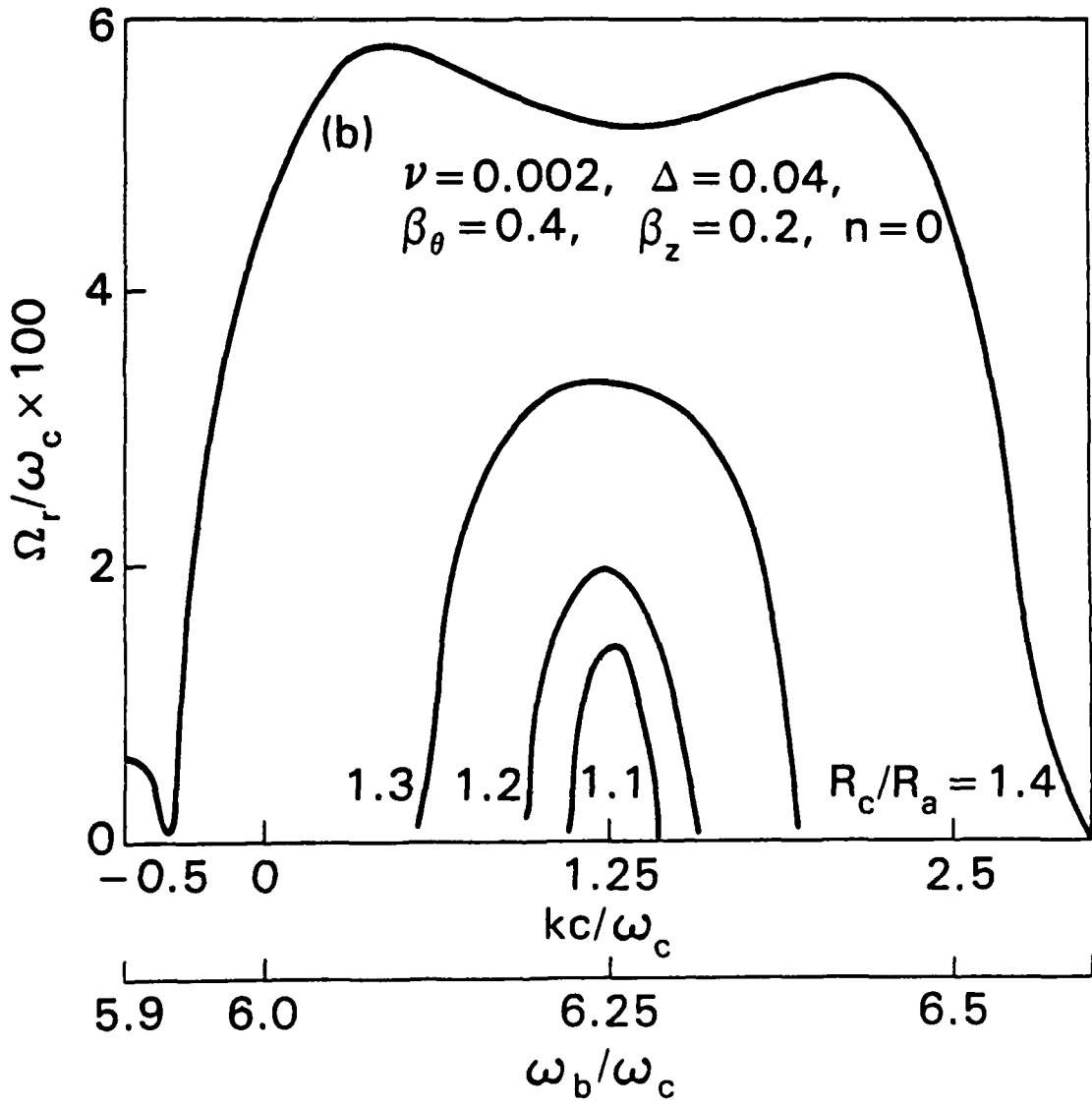


FIGURE 10. (CONTINUED)

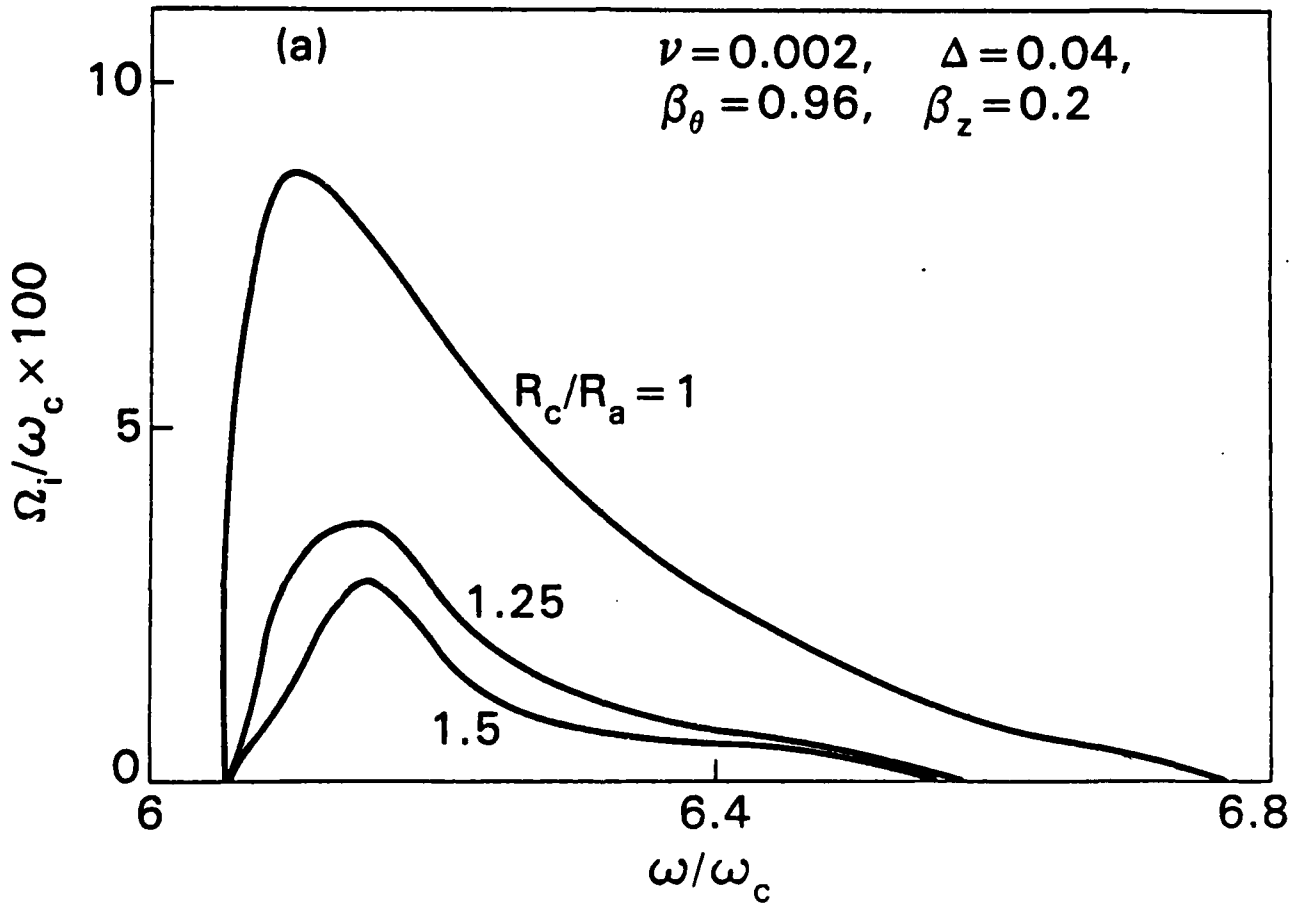


FIGURE 11. PLOTS OF (a) NORMALIZED GROWTH RATE Ω_i/ω_c AND (b) DOPPLER-SHIFTED REAL FREQUENCY Ω_r/ω_c VERSUS ω/ω_c FOR $\beta_\theta = 0.96$, THE GRAZING CONDITIONS CORRESPONDING TO EQ. (53), AND PARAMETERS OTHERWISE IDENTICAL TO FIGURE 8

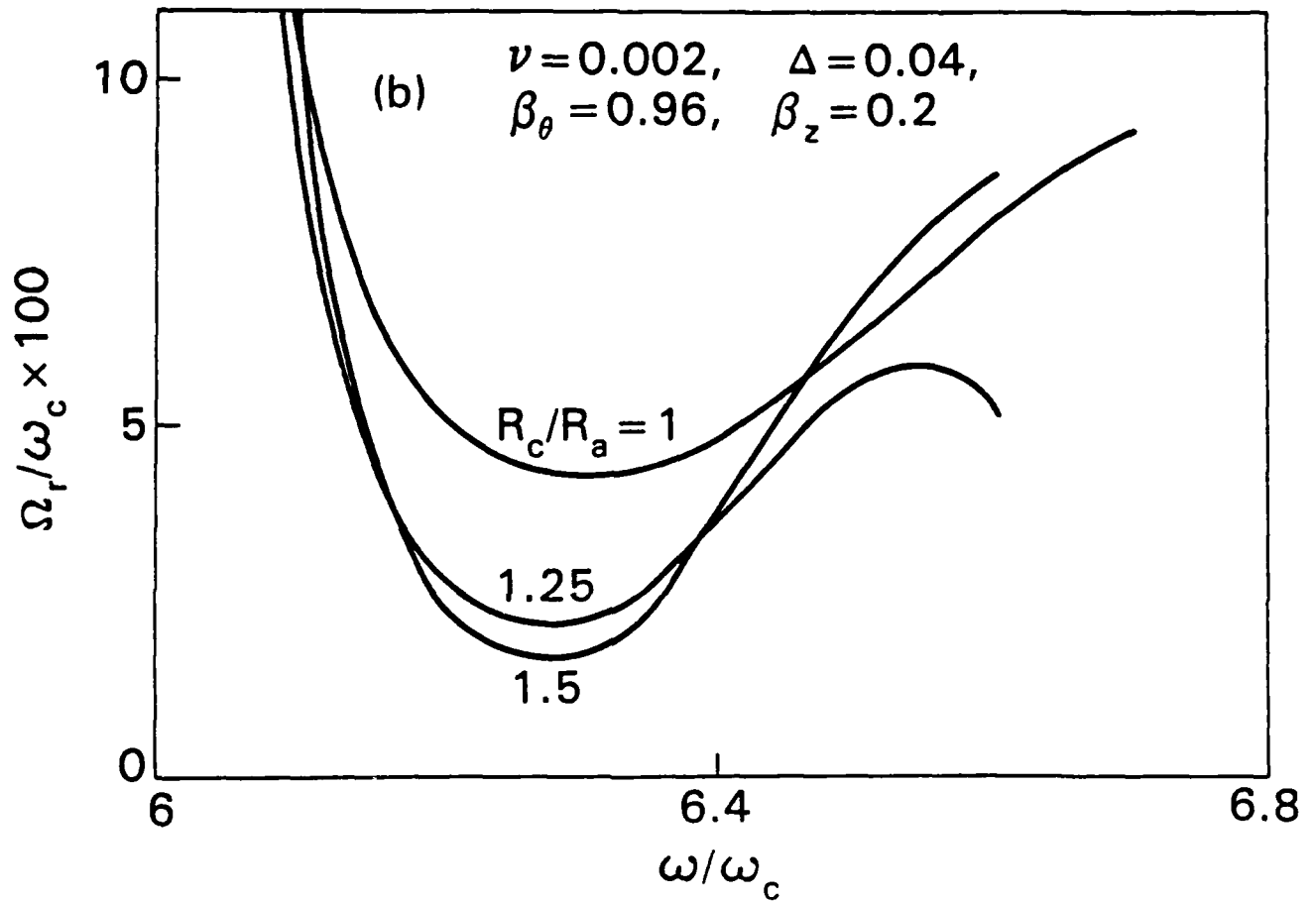


FIGURE 11. (CONTINUED)

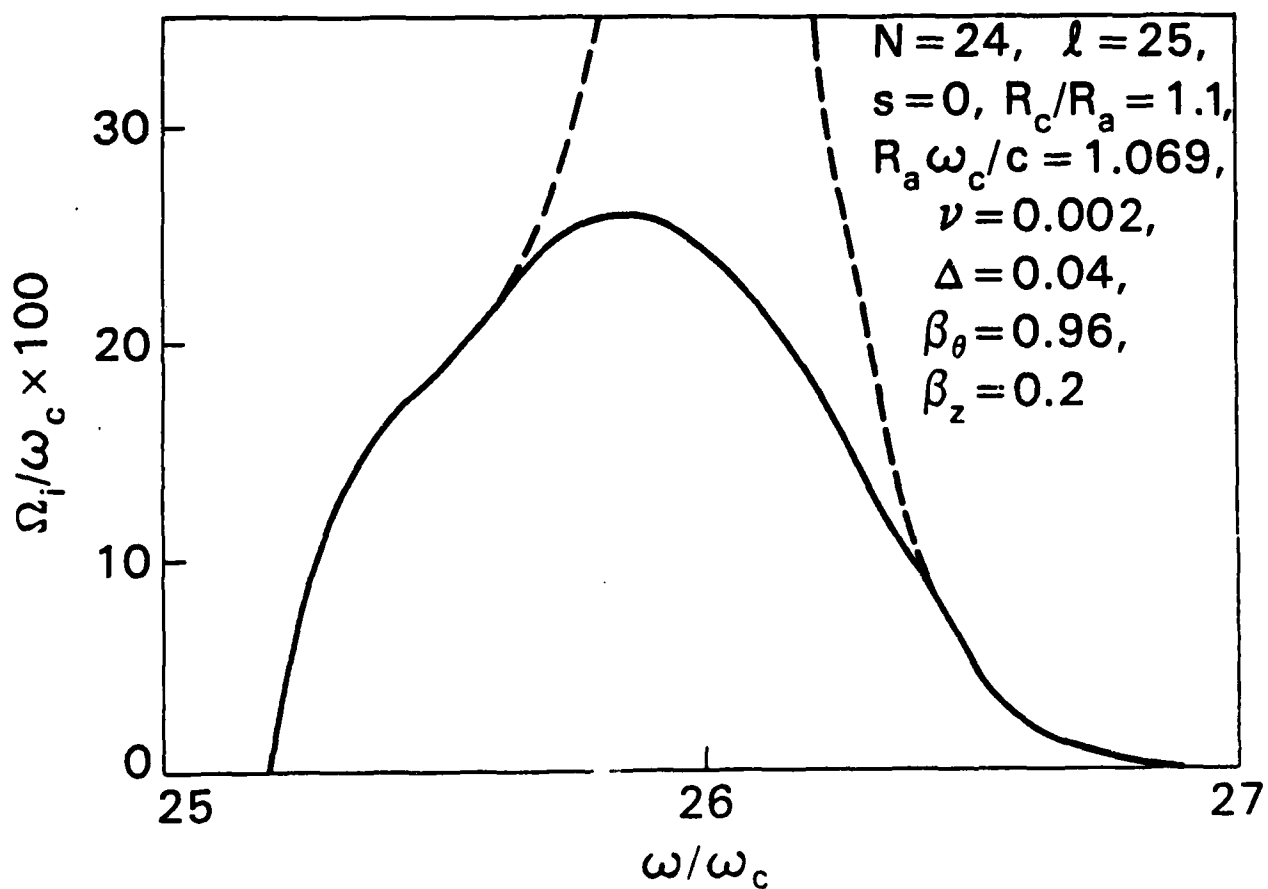


FIGURE 12. PLOT OF THE NORMALIZED GROWTH RATE Ω_i/ω_c VERSUS ω/ω_c OBTAINED FROM EQS. (47) AND (58) FOR $\beta_\theta = 0.96, N = 24, \ell = 25, R_c/R_a = 1.1, R_a\omega_c/c = 1.069, \alpha = \pi/2N,$ AND PARAMETERS OTHERWISE IDENTICAL TO FIGURE 8

REFERENCES

1. V. A. Flyagin, A. V. Gaponov, M. I. Petelin, and V. K. Yulpatov, IEEE Trans. Microwave Theory Tech. MTT-25, 514 (1977).
2. J. L. Hirschfield and V. L. Granatstein, IEEE Trans. Microwave Theory Tech. MTT-25, 528 (1977).
3. H. S. Uhm, R. C. Davidson and K. R. Chu, Phys. Fluids 21, 1877 (1978).
4. A. Palevsky and G. Bekefi, Phys. Fluids 22, 986 (1979).
5. D. A. G. Deacon, L. R. Elias, J. M. M. Madey, G. J. Ramian, H. A. Schwettman and T. I. Smith, Phys. Rev. Lett. 38, 897 (1977)
6. H. S. Uhm and R. C. Davidson, Phys. Fluids 24, 1541 (1981).
7. H. S. Uhm and R. C. Davidson, J. Appl. Phys. 49, 593 (1978).
8. W. W. Destler, D. W. Hudgings, M. J. Rhee, S. Kawasaki, and V. L. Granatstein, J. Appl. Phys. 48, 3291 (1977).
9. P. Sprangle, J. Appl. Phys. 47, 2935 (1978).
10. W. W. Destler, R. L. Weiler, and C. D. Strittler, Appl. Phys. Lett. 38, 570 (1981).
11. M. J. Rhee and W. W. Destler, Phys. Fluids 17, 1574 (1974).
12. H. S. Uhm and R. C. Davidson, Phys. Fluids 21, 265 (1978).
13. H. S. Uhm and R. C. Davidson, Phys. Fluids 20, 771 (1977).
14. N. M. Kroll and W. E. Lamb, Jr., J. Appl. Phys. 19, 166 (1948).
15. G. B. Collins, Microwave Magnetrons, (New York, McGraw-Hill Co., 1948) Chap. 2.
16. P. Sprangle and W. M. Manheimer, Phys. Fluids 18, 224 (1975).

APPENDIX A

Magnetic Wave Admittances

In this section, we obtain expressions for the wave admittances at the boundaries of an E-layer in a magnetron-type conductor. Shown in Fig. A-1 is one of the resonators in a magnetron-type conductor. Obviously, the electromagnetic field in the resonator is required to satisfy the boundary conditions

$$\begin{aligned} \hat{B}_r(r = R_c) = \hat{E}_z(r = R_c) = \hat{E}_\theta(r = R_c) = 0, \\ \hat{B}_\theta(\theta = \pm\alpha) = \hat{E}_z(\theta = \pm\alpha) = \hat{E}_r(\theta = \pm\alpha) = 0. \end{aligned} \quad (\text{A.1})$$

The previous study^{15,16} has shown that the lowest azimuthal mode in the resonator dominates the wave and beam interaction. Moreover, the theoretical analysis is considerably simplified when the electromagnetic field in the resonator is represented by the lowest azimuthal mode. Therefore, after a careful examination of the boundary conditions in Eq. (A.1), it is shown that the electric and magnetic fields in the resonator are expressed as

$$\hat{B}_z = b [J_0(pr) - J_1(\zeta)N_0(pr)/N_1(\zeta)] \exp \{ikz\} \quad , \quad (\text{A.2})$$

$$\hat{E}_\theta = ib(\omega/cp) [J_1(pr) - J_1(\zeta)N_1(pr)/N_1(\zeta)] \exp \{ikz\} \quad , \quad (\text{A.3})$$

$$\hat{B}_r = - (kc/\omega)\hat{E}_\theta \quad , \quad (\text{A.4})$$

for the TE mode and

$$\hat{E}_r = \hat{B}_\theta = \hat{E}_z = 0 \quad (\text{A.5})$$

for the TM mode. In Eq. (A.2), $J_\ell(x)$ and $N_\ell(x)$ are Bessel functions of the first and second kind, respectively, $\zeta = (\omega^2/c^2 - k^2)^{1/2} R_c$, and b is a constant. It is also emphasized that Eq. (A.5) is valid provided $\omega^2/c^2 - k^2 \neq 0$. Making use of Eq. (A.5), the electric wave admittances have been obtained in Eq. (34).

In the interaction region $0 \leq r \leq R_a$, the perturbed axial magnetic field is expressed as

$$\hat{B}_z = \begin{cases} \sum_{n=-\infty}^{\infty} b_{1n} J_n(pr) \exp \{ i(n\theta + kz) \} , \\ 0 \leq r < R_0 , \\ \sum_{n=-\infty}^{\infty} b_n Z_n(pr) \exp \{ i(n\theta + kz) \} , \\ R_0 < r \leq R_a , \end{cases} \quad (\text{A.6})$$

where the function $Z_n(pr)$ is defined by

$$Z_n(pr) = \begin{cases} J_n(pr) , & n \neq \ell , \\ J_\ell(pr) + G_\ell N_\ell(pr) , & n = \ell , \end{cases} \quad (\text{A.7})$$

and constant G_ℓ is determined from the proper boundary condition. From Eq. (A.3), we obtain the azimuthal electric field

$$\hat{E}_\theta(R_a^+) = -i(\omega/cp) [J_1(\eta) - J_1(\tau)N_1(\eta)/N_1(\tau)] \exp\{ikz\}, \quad (\text{A.8})$$

for

$$\frac{2\pi q}{N} - \alpha < \theta < \frac{2\pi q}{N} + \alpha$$

and $\hat{E}_\theta(R_a^+) = 0$, otherwise, where N is the number of the resonators, $q = 0, 1, \dots, N-1$, and $\psi(R_j^\pm)$ denotes $\lim_{\delta \rightarrow 0^+} \psi(R_j \pm \delta)$. It is also shown from Eq. (A.6) that

$$\hat{E}_\theta(R_a^-) = -i(\omega/cp) \sum_n b_n Z_n'(\eta) \exp\{i(n\theta + kz)\}, \quad (\text{A.9})$$

where the prime (') denotes $(d/dx)Z_n(x)$.

The constants b_n are determined by the average field matching^{15,16}

$$\begin{aligned} & \int_0^{2\pi} d\theta \hat{E}_\theta(R_a^-) \exp\{-in\theta\} \\ &= E_\theta(R_a^+) \sum_{q=0}^{N-1} \int_{(2\pi q/N) - \alpha}^{(2\pi q/N) + \alpha} d\theta \exp\{-in\theta\}, \end{aligned} \quad (\text{A.10})$$

which gives

$$b_n = b \frac{N\alpha}{\pi} \left(\frac{\sin n\alpha}{n\alpha} \right) \frac{1}{Z_n'(\eta)} \left[\frac{J_1(\tau)}{N_1(\tau)} N_1(\eta) - J_1(\eta) \right] \quad (\text{A.11})$$

for $n = s + mN$, and $b_n = 0$ otherwise, where m is any integer and $s = 0, 1, \dots, N-1$. Substituting Eq. (A.11) into Eq. (A.6), the axial magnetic field in $R_0 < r < R_a$ is expressed as

$$\hat{B}_z = b \frac{N\alpha}{\pi} \left[\frac{J_1(\zeta)}{N_1(\zeta)} N_1(\eta) - J_1(\eta) \right] \quad (\text{A.12})$$

$$\times \sum_{n=-\infty}^{\infty} \frac{Z_n(\text{pr})}{Z_n(\eta)} \left(\frac{\sin n\alpha}{n\alpha} \right) \exp \{i(n\theta + kz)\} .$$

Resonance is determined by the requirement that the average value of the axial magnetic field in the interaction region match that in the resonator, i.e.,

$$\int_{(2\pi q/N) - \alpha}^{(2\pi q/N) + \alpha} dB_z(R_a^-) = 2\alpha B_z(R_a^+) . \quad (\text{A.13})$$

Substituting Eqs. (A.2) and (A.12) into Eq. (A.13), and carrying out a tedious but straightforward algebra, we determine the constant G_ℓ

$$G_\ell(\omega, k) = - \frac{J_\ell'(\eta) D(\omega, k)}{N_\ell'(\eta) F(\omega, k)} \quad (\text{A.14})$$

where the vacuum dispersion function $D(\omega, k)$ is defined by

$$D(\omega, k) = \sum_{n=-\infty}^{\infty} \frac{J_n(\eta)}{J_n'(\eta)} \left(\frac{\sin n\alpha}{n\alpha} \right)^2 \quad (\text{A.15})$$

$$- \frac{\pi}{N\alpha} \frac{J_0(\eta)N_1(\zeta) - J_1(\zeta)N_0(\eta)}{J_1(\zeta)N_1(\eta) - J_1(\eta)N_1(\zeta)}$$

and the function $F(\omega, k)$ is given by

$$F(\omega, k) = D(\omega, k) - \left[\frac{J'_\ell(\eta)}{J_\ell(\eta)} - \frac{N'_\ell(\eta)}{N_\ell(\eta)} \right] \left(\frac{\sin l\alpha}{l\alpha} \right)^2 \quad (\text{A.16})$$

The perturbed axial magnetic field with azimuthal harmonic number l is given by

$$\hat{B}_{lz}(r) = \begin{cases} b_{1l} J_\ell(\rho r) & , \quad 0 \leq r < R_0, \\ b_l \left[J_\ell(\rho r) + G_l N_\ell(\rho r) \right] & , \quad R_0 < r \leq R_a, \end{cases} \quad (\text{A.17})$$

from Eq. (A.6). Making use of Eq. (A.17) and the definitions of the magnetic wave admittances in Eq. (12), it can be shown that sum of the magnetic wave admittances at $r = R_0$ is expressed as

$$b_- + b_+ = \frac{2lG_l/\pi\xi^2 J'_\ell(\xi)}{J'_\ell(\xi) + G_l N'_\ell(\xi)}, \quad (\text{A.18})$$

where $\xi = \zeta R_0/R_c = \eta R_0/R_a = (\omega^2/c^2 - k^2)^{1/2} R_0$.

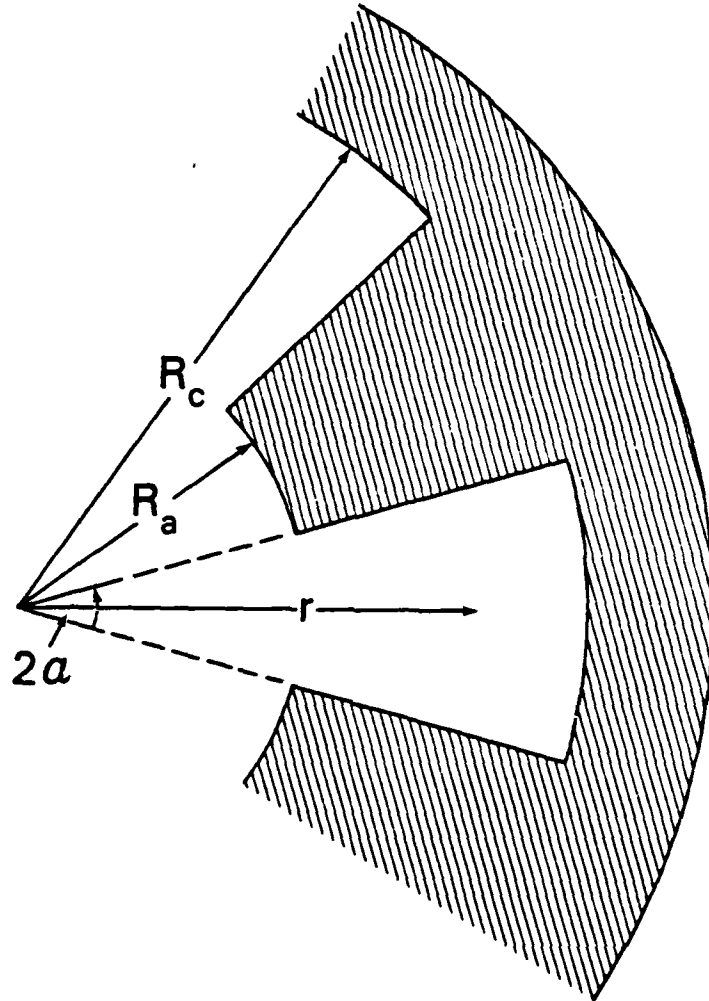


FIGURE A-1. CONFIGURATION OF A RESONATOR

DISTRIBUTION

	<u>Copies</u>		<u>Copies</u>
Dr. Richard E. Aamodt Science Application Inc. 934 Pearl St. Suite A Boulder, CO 80302	1	Dr. J. Bayless DARPA Attn: DEO 1400 Wilson Blvd. Arlington, VA 22209	1
Dr. Saeyoung Ahn Code 5205 Naval Research Lab. Washington, D.C. 20375	1	Dr. Robert Behringer ONR 1030 E. Green Pasadena, CA 91106	1
Dr. Wahab A. Ali Naval Research Lab. Code 4700 4555 Overlook Ave., S.W. Washington, D.C. 20375	1	Prof. George Bekefi Bldg. 36-213, MIT 77 Massachusetts Ave. Cambridge, MA 02139	1
Dr. Donald Arnush TRW, Plasma Physics Dept. R1/107 1 Space Park Rodondo Beach, CA 90278	1	Dr. Gregory Benford Physics Department University of California Irvine, CA 92717	1
Dr. J.M. Baird Code 4740 (B-K Dynamics) Naval Research Lab. 4555 Overlook Ave., S.W. Washington, D.C. 20375	1	Dr. Jim Benford Physics International Co. 2700 Merced St. San Leandro, CA 94577	1
Dr. William A. Barletta Lawrence Livermore National Lab. L-321 University of California Livermore, CA 94550	1	Dr. Kenneth D. Bergeron Plasma Theory Div. - 5241 Sandia Laboratories Albuquerque, NM 87115	1
Dr. L. Barnett Code 4740 (B-K Dynamics) Naval Research Lab. 4555 Overlook Ave., S.W. Washington, D.C. 20375	1	Dr. T. Berlincourt Office of Naval Research Department of the Navy Arlington, VA 22217	1

DISTRIBUTION (Cont.)

	<u>Copies</u>		<u>Copies</u>
Dr. I. B. Bernstein Yale University Mason Laboratory 400 Temple Street New Haven, CT 06520	1	Dr. Neal Carron Mission Research Corp. 735 State Street Santa Barbara, CA 93102	1
Dr. O. Book Code 4040 Naval Research Laboratory Washington, D.C. 20375	1	Dr. Frank Chambers Lawrence Livermore National Lab. L-321 University of California Livermore, CA 94550	1
Dr. Jay Boris Naval Research Lab. Code 4040 4555 Overlook Ave., S.W. Washington, D.C. 20375	1	Prof. F. Chen Dept. of E. E. UCLA Los Angeles, CA 90024	1
Dr. Howard E. Brandt Harry Diamond Labs 2800 Powder Mill Road Adelph, MD 20783	1	Dr. M. Caponi TRW Advance Tech. Lab. 1 Space Park Redondo Beach, CA 90278	1
Dr. R. Briggs Lawrence Livermore Lab. P.O. Box 808 Livermore, CA 94550	1	Dr. K. R. Chu Naval Research Lab. Code 4740 4555 Overlook Ave., S.W. Washington, D.C. 20375	1
Dr. K. Brueckner La Jolla Institute P.O. Box 1434 La Jolla, CA 92038	1	Dr. Timothy Coffey Naval Research Lab. 4555 Overlook Ave., S.W. Washington, D.C. 20375	1
Dr. Herbert L. Buchanan Lawrence Livermore National Lab L-321 University of California Livermore, CA 94550	1	Dr. W. J. Condell Office of Naval Research Code 421 Department of the Navy Arlington, VA 22217	1
Dr. K. J. Button Massachusetts Institute of Technology Francis Bitter National Magnet Laboratory Cambridge, MA 02139	1	Dr. G. Cooperstein Naval Research Lab. Washington, D.C. 20375	1
		Dr. Edward Cornet W.J. Schafer Associates, Inc. 1901 North Fort Myer Dr. Arlington, VA 22209	1

DISTRIBUTION (Cont.)

	<u>Copies</u>		<u>Copies</u>
Prof. R. Davidson Plasma Fusion Center Massachusetts Inst. of Technology Cambridge, MA 02139	1	Dr. D. Eccleshall U.S. Army Ballistic Research Lab. Aberdeen Proving Ground, MD 21005	1
Dr. J. Dawson Dept. of Physics UCLA Los Angeles, CA 90024	1	Dr. Barbara Epstein Sandia Laboratories Albuquerque, NM 87185	1
Dr. W. Destlar Dept. of Electrical Engineering University of Maryland College Park, MD 20742	1	Dr. A. Fisher Physics Dept. University of California Irvine, CA 92664	1
Prof. R. Diament Columbia University Dept. of Electrical Engineering New York, NY 10027	1	Dr. R. J. Faehl Los Alamos Scientific Lab. Los Alamos, NM 87544	1
Prof. W. Doggett NC State University P.O. Box 5342 Raleigh, NC 27650	1	Dr. Leon Feinstein Science Applications, Inc. 5 Palo Alto Square Palo Alto, CA 94304	1
Dr. H. Dreicer Plasma Physics Division Los Alamos Scientific Lab. Los Alamos, NM 87544	1	Dr. Franklin Felber Western Research Corporation 8616 Commerce Ave. San Diego, CA 92121	1
Dr. A. Drobot Naval Research Laboratory Code 4790 (SAI) Washington, D.C. 30275	1	Dr. Richard Fernsler Code 4770 Naval Research Lab. 4555 Overlook Ave., S.W. Washington, D.C. 20375	1
Prof. W. E. Drummond Austin Research Associates 1901 Rutland Drive Austin, TX 78758	1	Dr. Thomas Fessenden Lawrence Livermore National Lab. L-321 University of California Livermore, CA 94550	1
Prof. H. H. Fleischmann Lab. for Plasma Studies and School of Applied and Engr. Physics Cornell University Ithaca, NY 14850	1		

DISTRIBUTION (Cont.)

	<u>Copies</u>		<u>Copies</u>
Dr. Robert Fossum, Director DARPA 1400 Wilson Boulevard Arlington, VA 22209	1	Dr. Robert Greig Naval Research Lab. (Code 4763) 4555 Overlook Ave., S.W. Washington, D.C. 20375	1
Dr. H. Freund Naval Research Lab. Code 4790 4555 Overlook Ave., S.W. Washington, D.C. 20375	1	Dr. J.U. Guillory Jaycor 20050 Whiting St. Suite 500 Alexandria, VA 22304	1
Dr. M. Friedman Code 4700.1 Naval Research Laboratory Washington, D.C. 20375	1	Dr. Irving Haber Code 4790 Naval Research Lab. Washington, D.C. 20375	1
Dr. B. Godfrey Mission Res. Corp. 1400 San Mateo Blvd, S.E. Suite A Albuquerque, NM 87108	1	Prof. D. Hammer Lab. of Plasma Studies Cornell University Ithaca, NY 14850	1
Dr. T. Godlove Office of Inertial Fusion U.S. Department of Energy Washington, D.C. 20545	1	Dr. Robert Hill Physics Division, #341 National Science Foundation Washington, D.C. 20550	1
Dr. Jeffry Golden Naval Research Laboratory Washington, D.C. 20375	1	Dr. J. L. Hirshfield Yale University Mason Laboratory 400 Temple Street New Haven, CT 06520	1
Dr. S. Goldstein Jaycor (Code 4770) Naval Research Lab. Washington, D.C. 20375	1	Dr. Richard Hubbard Code 4790 (Jaycor) Naval Research Lab. 4555 Overlook Ave., S.W. Washington, D.C. 20375	1
Dr. Victor Granatstein Naval Research Lab. Washington, D.C. 20375	1	Dr. Bertram Hui Naval Research Lab. Code 4790 4555 Overlook Ave., S.W. Washington, D.C. 20375	1
Dr. S. Graybill Harry Diamond Lab. 2800 Powder Mill Rd. Adelphi, MD 20783	1	Dr. S. Humphries Sandia Laboratories Albuquerque, NM 87115	1
Dr. Michael Greenspan McDonnell Douglas Corp. St. Louis, MO 63166	1		

DISTRIBUTION (Cont.)

	<u>Copies</u>		<u>Copies</u>
Dr. Robert Johnston Science Applications, Inc. 5 Palo Alto Square Palo Alto, CA 94304	1	Dr. Kwang Je Kim Bldg. 64 #223 A & FR Div. Lawrence Berkeley Lab. Berkeley, CA 94720	1
Dr. Howard Jory Varian Associates, Bldg. 1 611 Hansen Way Palo Alto, CA 94303	1	Dr. Jin Joong Kim North Carolina State University Raleigh, NC 27607	1
Dr. Glenn Joyce Code 4790 Naval Research Lab. 4555 Overlook Ave., S.W Washington, D.C. 20375	1	Prof. N. M. Kroll La Jolla Institutes P.O. Box 1434 La Jolla, CA 92038	1
Dr. Selig Kainer Naval Research Lab. 4555 Overlook Ave., S.W. Washington, D.C. 20375	1	Dr. M. Lampe Naval Research Lab. Code 4790 4555 Overlook Ave., S.W. Washington, D.C. 20375	1
Dr. C.A. Kapetanacos Plasma Physics Division Naval Research Laboratory Washington, D.C. 20375	1	Dr. L. J. Laslett Lawrence Berkeley Lab. 1 Cyclotron Road Berkeley, CA 96720	1
Dr. Denis Keefe Lawrence Berkeley Lab. 1 Cyclotron Road Berkeley, CA 94720	1	Dr. Y. Y. Lau Naval Research Lab. Code 4740 (SAI) 4555 Overlook Ave., S.W. Washington, D.C. 20375	1
Dr. Douglas Keeley Science Applications, Inc. 5 Palo Alto Square Palo Alto, CA 94304	1	Dr. Glen R. Lambertson Lawrence Berkeley Lab. 1 Cyclotron Road, Bldg. 47 Berkeley, CA 94720	1
Dr. Hogil Kim A & FR Div. Lawrence Berkeley Lab. Berkeley, CA 94720	1	Dr. J. Carl Leader McDonnell Douglas Corp. Box 516 St. Louis, MO 63166	1
Dr. Hong Chul Kim A & FR Div. Lawrence Berkeley Lab. Berkeley, CA 94720	1		

DISTRIBUTION (Cont.)

	<u>Copies</u>		<u>Copies</u>
Dr. W. M. Manheimer Naval Research Lab. Code 4790 4555 Overlook Ave., S. W. Washington, D. C. 20375	1	Dr. James Mark L-477 Lawrence Livermore Lab Livermore, CA 94550	1
Dr. Edward P. Lee Lawrence Livermore National Lab L-321 University of California Livermore, CA 94550	1	Dr. Jon A. Masamitsu Lawrence Livermore National Lab L-321 University of California Livermore, CA 94550	1
Dr. Ray Lemke Air Force Weapons Lab Kirtland Air Force Base Albuquerque, NM 87117	1	Dr. Bruce R. Miller Div. 5246 Sandia Laboratories Albuquerque, NM 87115	1
Dr. Anthony T. Lin University of California Los Angeles, CA 90024	1	Dr. Melvin Month Department of Energy High Energy Physics Washington, D.C. 20545	1
Dr. C. S. Liu Dept. of Physics University of Maryland College Park, MD 20742	1	Dr. Philip Morton Stanford Linear Accelerator Center P.O. Box 4349 Stanford, CA 94305	1
Dr. Tom Lockner Sandia Laboratories Albuquerque, NM 87115	1	Dr. Don Murphy Naval Research Lab 4555 Overlook Ave., S.W. Washington, D.C. 20375	1
Dr. Conrad Longmire Mission Research Corp. 735 State Street Santa Barbara, CA 93102	1	Dr. Won Namkung E. E. Department University of Maryland College Park, MD 20742	1
Prof. R. V. Lovelace School of Applied and Eng. Physics Cornell University Ithaca, NY 14853	1	Prof. J. Nation Lab of Plasma Studies Cornell University Ithaca, NY 14850	1
Dr. Joseph A. Mangano DARPA 1400 Wilson Blvd. Arlington, VA 22209	1	Dr. V. Kelvin Neil Lawrence Livermore Nat'l Lab P.O. Box 808, L-321 Livermore, CA 94550	1

DISTRIBUTION (Cont.)

	<u>Copies</u>		<u>Copies</u>
Dr. Barry Newberger Mail Stop 608 Los Alamos National Lab Los Alamos, NM 87544	1	Dr. R. Post Lawrence Livermore Lab University of California P.O. Box 808 Livermore, CA 94550	1
Dr. C. L. Olson Sandia Lab Albuquerque, NM 87115	1	Dr. D. S. Prono Lawrence Livermore Lab P.O. Box 808 Livermore, CA 94550	1
Dr. Edward Ott Dept. of Physics University of Maryland College Park, MD 20742	1	Dr. S. Putnam Physics Internal Co. 2700 Merced St. San Leandro, CA 94577	1
Dr. Peter Palmadesso Bldg A50 #107 Naval Research Lab Washington, D.C. 20375	1	Dr. Sid Putnam Pulse Sciences, Inc. 1615 Broadway, Suite 610 Oakland, CA 94612	1
Dr. Ron Parkinson Science Applications, Inc. 1200 Prospect St. P.O. Box 2351 La Jolla, CA 92038	1	Dr. Michael Raleigh Naval Research Lab Code 4763 4555 Overlook Ave., S.W. Washington, D.C. 20375	1
Dr. Richard Patrick AVCO - Everett Research Lab, Inc. 2385 Revere Beach Pkwy Everett, MA 02149	1	Dr. M. E. Read Naval Research Lab Code 4740 4555 Overlook Ave., S.W. Washington, D.C. 20375	1
Dr. Robert Pechacek Naval Research Lab Code 4763 4555 Overlook Ave., S.W. Washington, D.C. 20375	1	Prof. M. Reiser Dept. of Physics & Astronomy University of Maryland College Park, MD 20742	1
Dr. Sam Penner National Bureau of Standards Bldg. 245 Washington, D.C. 20234	1	Dr. M. E. Rensink Lawrence Livermore Lab P.O. Box 808 Livermore, CA 94550	1
Dr. Michael Picone Naval Research Lab 4555 Overlook Ave., S.W. Washington, D.C. 20375	1	Dr. Moon-Jhong Rhee E. E. Department University of Maryland College Park, MD 20742	1

DISTRIBUTION (Cont.)

	<u>Copies</u>		<u>Copies</u>
Dr. C. W. Roberson Naval Research Lab Code 4740 4555 Overlook Ave., S.W. Washington, D.C. 20375	1	Dr. William Sharp Naval Research Lab Code 4790 (SAI) 4555 Overlook Ave., S.W. Washington, D.C. 20375	1
Dr. J. A. Rome Oak Ridge National Lab Oak Ridge, TN 37850	1	Dr. D. Straw AFWL Kirtland AFB, NM 87117	1
Dr. Marshall N. Rosenbluth University of Texas at Austin Inst. for Fusion Studies RLM 11.218 Austin, TX 78712	1	Dr. John Siambis Science Applications, Inc. 5 Palo Alto Square Palo Alto, CA 94304	1
Prof. Norman Rostoker Dept. of Physics University of California Irvine, CA 92664	1	Dr. J. S. Silverstein Code 4740 (HDL) Naval Research Lab 4555 Overlook Ave., S.W. Washington, D.C. 20375	1
Dr. C. F. Sharn Naval Sea Systems Command Department of the Navy Washington, D. C. 20363	1	Dr. M. Lee Sloan Austin Research Associates, Inc. 1901 Rutland Drive Austin, Texas 78758	1
Prof. S. F. Schlesinger Columbia University Dept. of Electrical Engineering New York, NY 10027	1	Dr. L. Smith Lawrence Berkeley Lab 1 Cyclotron Road Berkeley, CA 94770	1
Prof. George Schmidt Physics Dept. Stevens Institute of Technology Hoboken, NJ 07030	1	Dr. Joel A. Snow Senior Technical Advisor Office of Energy Research U.S. Department of Energy, M.S. E084 Washington, D.C. 20585	1
Dr. Andrew M. Sessler Lawrence Berkeley Lab Berkeley, CA 94720	1	Dr. Philip Sprangle Naval Research Lab Code 4790 4555 Overlook Ave., S.W. Washington, D.C. 20375	1
Dr. J. D. Sethian Naval Research Lab Code 4762 Washington, D.C. 20375	1		

DISTRIBUTION (Cont.)

	<u>Copies</u>		<u>Copies</u>
Dr. Doug Strickland Naval Research Lab Code 4790 (Beers) 4555 Overlook Ave., S W. Washington, D.C. 20375	1	Dr. John E. Walsh Department of Physics Dartmouth College Hanover, NH 03755	1
Dr. Charles D. Striffler E. E. Dept. Univ. of Maryland College Park, MD 20742	1	Dr. Wasneski Naval Air Systems Command Department of the Navy Washington, D.C. 20350	1
Prof. R. Sudan Lab of Plasma Studies Cornell University Ithaca, NY 14850	1	Dr. N. R. Vanderplaats Naval Research Laboratory Code 6805 4555 Overlook Ave., S. W. Washington, D.C. 20375	1
Dr. C. M. Tang Naval Research Lab Code 4790 4555 Overlook Ave., S.W. Washington, D.C. 20375	1	Lt. Col. W. Whitaker Defense Advanced Research Projects Agency 1400 Wilson Boulevard Arlington, VA 22209	1
Dr. R. Temkin Plasma Fusion Center Massachusetts Institute of Technology Cambridge, MA 02139	1	Dr. Mark Wilson National Bureau of Standards Gaithersburg, MD 20760	1
Dr. Lester E. Thode Mail Stop 608 Los Alamos National Lab Los Alamos, NM 87544	1	Dr. Gerold Yonas Sandia Lab Albuquerque, NM 87115	1
Dr. James R. Thompson Austin Research Associate, Inc. 1901 Rutland Drive Austin, Texas 78758	1	Dr. Simon S. Yu Lawrence Livermore National Lab L-321 University of California Livermore, CA 94550	1
Dr. D. Tidman Jaycor 205 S. Whiting St. Alexandria, VA 22304	1	Defense Technical Information Center Cameron Station Alexandria, VA 22314	12
Dr. A. W. Trivelpiece Science Applications, Inc. San Diego, CA 92123	1	<u>Internal distribution:</u> R R04 R40	 1 1 1

DISTRIBUTION (Cont.)

CopiesInternal Distribution (Cont.)

R401	1
R43 (C. W. Lufcy)	1
R44 (T. F. Zien)	1
R45 (H. R. Riedl)	1
R13 (J. Forbes)	1
R41 (P. O. Hesse)	1
R41 (R. Cawley)	1
R41 (M. H. Cha)	1
R41 (H. C. Chen)	1
R41 (J. Y. Choe)	1
R41 (R. Fiorito)	1
R41 (O. F. Goktepe)	1
R41 (M. J. Rhee)	1
R41 (D. W. Rule)	1
R41 (Y. C. Song)	1
R41 (H. S. Uhm)	1
R43 (A. D. Krall)	1
F	1
F14 (H. C. Coward)	1
F40 (J. F. Cavanagh)	1
F10 (K. C. Baile)	1
F46 (D. G. Kirkpatrick)	1
F34 (R. A. Smith)	1
F34 (E. Nolting)	1
F34 (V. L. Kenyon)	1
F04 (M. F. Rose)	1
F34 (F. Sazama)	1
N14 (R. Biegalski)	1
E431	9
E432	3
E35	1

4-
DT